Applications of Mid-infrared Frequency Combs for Linear and Nonlinear Vibrational Spectroscopy

Juho Karhu

University of Helsinki
Faculty of Science
Department of Chemistry
A.I. Virtasen aukio 1 (P.O. Box 55)
FI-00014 University of Helsinki
Finland

Doctoral dissertation, to be presented for public discussion with the permission of the Faculty of Science of the University of Helsinki, in Auditorium A110, Department of Chemistry (A.I. Virtasen aukio 1, Helsinki), on the 4th of June, 2019 at 12 o'clock.

Supervisor

Prof. Lauri Halonen
Department of Chemistry
University of Helsinki
Helsinki, Finland

Instructors

Prof. Markku Vainio
Department of Chemistry
University of Helsinki
Helsinki, Finland

Dr. Markus Metsälä
Department of Chemistry
University of Helsinki
Helsinki, Finland

Reviewers

Professor Emeritus Jouko Korppi-Tommola
Department of Chemistry
University of Jyväskylä
Jyväskylä, Finland

Prof. Tapio Niemi
Laboratory of Photonics
Tampere University
Tampere, Finland

Opponent

Prof. Stephan Schlemmer
Department of Physics
University of Cologne
Cologne, Germany

ISBN 978-951-51-5260-2 (paperback)
ISBN 978-951-51-5261-9 (PDF)
`http://ethesis.helsinki.fi`
Unigrafia Helsinki 2019

Abstract

The mid-infrared wavelength range is important for vibrational spectroscopy and trace gas detection, because it contains strong fundamental vibrational transitions. The extension of spectroscopic techniques into the mid-infrared wavelengths is a major area of development. This thesis describes sensitive spectroscopic measurements, which take advantage of the strong mid-infrared transitions to produce novel spectral data. The measurement setups are enhanced using optical frequency combs. Frequency combs are stable laser sources, which emit laser light over a wide optical spectrum. Their development was awarded with one half of the Nobel Prize in Physics in the year 2005. Frequency combs have found many applications in laser spectroscopy, because they combine the coherence and high brightness of a laser source with a wide optical spectrum. The stability of the frequency combs is valuable in high-resolution spectroscopy and metrology.

This thesis is focused on two novel measurements: direct frequency comb spectroscopy of radiocarbon methane and double resonance spectroscopy of acetylene. In the former measurement, an optical frequency comb emitting in the mid-infrared region was used as the light source in broadband spectroscopy of radiocarbon methane. The carbon atom in the radiocarbon methane molecule is replaced by the radioactive carbon-14 isotope. High sensitivity was reached by combining a high-power mid-infrared frequency comb with cantilever-enhanced photoacoustic spectroscopy. The photoacoustic detector can take full advantage of the high power spectral density of the frequency comb. This measurement produced the first reported infrared spectrum of radiocarbon methane.

In the double resonance spectroscopy measurements, a mid-infrared and a near-infrared light source were simultaneously used to excite two transitions of acetylene, with a shared energy state. This allows detection of spectral lines, which are normally absent in an acetylene infrared spectrum. The method also provides sub-Doppler resolution for determining spectral line positions with high precision. Because of the sub-Doppler resolution, instabilities of the light sources can begin to limit the precision of the measurements. A drastic increase in sensitivity was reached by stabilizing the light sources using frequency combs as references.

Acknowledgements

First, I would like to thank Professor Lauri Halonen for sparking my interest in laser spectroscopy, for the bulk of my physical chemistry education and the long-standing support you have shown throughout my academic career so far. I would like to extend my thanks to the rest of my instructors: Professor Markku Vainio and Doctor Markus Metsälä. Without your support and expert guidance, this work would not have been possible. I am also thankful to all of my colleagues, past and present, at the Laser Spectroscopy Group and what was the Laboratory of Physical Chemistry. The outstanding people and the friendly atmosphere made for an excellent work environment.

The work done in this thesis has involved the collaboration of many people and I greatly appreciate the contributions of all of my coauthors. I am grateful for the financial support from the doctoral programme in chemistry and molecular sciences at the University of Helsinki.

Furthermore, I would like thank my friends for all the support and the much-appreciated moments of respite throughout this long journey. I would also like to express my gratitude to all of my family, especially my parents Kaija and Pentti, for all the love and support you have shown throughout my studies and this thesis work.

Helsinki, May 2019

Juho Karhu

List of publications

I J. Karhu, J. Nauta, M. Vainio, M. Metsälä, S. Hoekstra, L. Halonen, "Double resonant absorption measurement of acetylene symmetric vibrational states probed with cavity ring down spectroscopy," The Journal of Chemical Physics, **144**(24), 244201 (2016)

II M. Vainio, J. Karhu, "Fully stabilized mid-infrared frequency comb for high-precision molecular spectroscopy," Optics Express, **25**(4), 4190 – 4200 (2017)

III J. Karhu, M. Vainio, M. Metsälä, L. Halonen, "Frequency comb assisted two-photon vibrational spectroscopy," Optics Express, **25**(5), 4688 – 4699 (2017)

IV J. Karhu, K. Lehmann, M. Vainio, M. Metsälä, L. Halonen, "Step-modulated decay cavity ring-down detection for double resonance spectroscopy," Optics Express, **26**(22), 29086 – 2998 (2018)

V J. Karhu, T. Tomberg, F. Senna Vieira, G. Genoud, V. Hänninen, M. Vainio, M. Metsälä, T. Hieta, S. Bell, L. Halonen, "Broadband photoacoustic spectroscopy of $^{14}CH_4$ with a high-power mid-infrared optical frequency comb," Optics Letters **44**(5), 1142 – 1145 (2019)

The author has prepared the manuscripts in publications I, III and V, and the parts of the manuscript related to the experimental work in publication IV. The author has contributed to the building of the experimental setup and performed the measurements presented in publication I, and interpreted the measured data. The author has established the locking between the frequency comb and the CW-OPO in article II, and performed the saturation spectroscopy measurement. The author has designed and built the experimental arrangement in publications III, and performed the measurements and data analysis. The author has designed the practical implementation of the experimental setup in publication IV, performed measurements and interpreted the experimental data. The author has contributed to the design of the measurement setup used in publications V, planned and performed the measurements, and analyzed the experimental results.

Glossary

AMS	accelerator mass spectrometer
AOM	acousto-optic modulator
CEPAS	cantilever-enhanced photoacoustic spectroscopy
CRDS	cavity ring-down spectroscopy
CW	continuous-wave
DRO	doubly resonant optical parametric oscillator
DROC	doubly resonant optical parametric oscillator comb
ECDL	external cavity diode laser
FTS	Fourier-transform spectrometer
GS	ground state
HHG	half harmonic generation
LO	local oscillator
OFC	optical frequency comb
OPO	optical parametric oscillator
PAS	photoacoustic spectroscopy
PID	proportional-integral-derivative
PPLN	periodically poled lithium niobate
ppm	parts per million
ppq	parts per quadrillion
QEPAS	quartz tuning fork enhanced photoacoustic spectroscopy
QPM	quasi phase matching
QTF	quartz tuning fork
SHG	second harmonic generation
SNR	signal-to-noise ratio
SPO	synchronously pumped optical parametric oscillator
SRO	singly resonant optical parametric oscillator
SROC	singly resonant optical parametric oscillator comb

Contents

1 Introduction **1**

2 Rovibrational spectroscopy **4**
2.1 Transition line shape 7

3 Mid-infrared laser sources **10**
3.1 Optical parametric oscillator 10
3.2 Optical frequency combs 13
3.2.1 Mode locking 14
3.2.2 Full stabilization 15
3.3 Mid-infrared frequency combs 16
3.3.1 Synchronously pumped optical parametric oscillator 17

4 Absorption spectroscopy methods **19**
4.1 Cavity ring-down spectroscopy 19
4.2 Photoacoustic spectroscopy 22
4.2.1 Fourier-transform photoacoustic spectroscopy 24
4.2.2 Direct comb photoacoustic spectroscopy of $^{14}CH_4$ 26

5 Nonlinear spectroscopy **31**
5.1 Saturation spectroscopy 31
5.1.1 Hole burning 32
5.1.2 Lamb dip 33
5.1.3 Comb-assisted Lamb dip spectroscopy of CH_4 34
5.2 Double resonance spectroscopy 36
5.2.1 Cavity ring-down double resonance spectroscopy of C_2H_2 . . . 38
5.2.2 Background suppression in double resonance cavity ring-down spectroscopy 42
5.2.3 Frequency comb assisted double resonance spectroscopy of C_2H_2 44

6 Conclusions **47**

Chapter 1

Introduction

Molecular spectroscopy in the infrared region can be used to study the structure and dynamics of molecules. The transitions excited by infrared radiation are related to changes in vibrational and rotational movement of molecules. Due to quantization of the related energies, the transitions show up in an infrared spectrum as discrete transition lines. The wavelength, shape, and intensity of the lines reveal information about the structure and dynamics of the molecule, such as lengths of its bonds, the symmetry of the molecule, and the energy transfer between the different modes of intramolecular movement.

High-resolution infrared spectroscopy has found many useful applications, most notably in identification and quantification of molecules in sample mixtures. The wavelengths of the infrared transition lines depend on the structure of the absorbing molecule, and therefore, each molecule has its own characteristic infrared spectrum. In the gas phase, the transition lines are often narrow and well separated, so that it is possible to distinguish transitions of different molecules from each other. The absorption strength is proportional to the concentration of the absorbing molecule. By measuring absorbance at a wavelength corresponding to a transition line of a known molecule, the concentration of that molecule can be calculated. The most sensitive spectroscopic methods can reach the limit of detection at the part-per-quadrillion (ppq) level [1]. That is, a molecule of the analyte for every 10^{15} molecules of the sample gas can be detected. Realizing spectrometers with ever lower detection limits is an active area of development in infrared spectroscopy. Two detection methods have especially become widely used due to their simplicity and high sensitivity, namely cavity ring-down spectroscopy (CRDS) [2] and photoacoustic spectroscopy (PAS) [3]. These techniques are described later in this thesis.

One area of interest is the development and application of novel light sources in spectroscopy. The invention of lasers revolutionized many areas of spectroscopy [4]. For example, the high spatial coherence of the laser beam allows using long interaction paths with multipass cells, the high brightness of laser light often leads to increased sensitivity, and narrow linewidth lasers can be coupled efficiently into optical cavities. The last item has led to the development of sensitive cavity enhanced spectroscopy methods [5]. Lasers have also made possible the observation of many nonlinear phenomena, which require high optical intensities [6, 7]. The advances in nonlinear optics

have led to the development of laserlike coherent light sources called optical parametric oscillators (OPO), which have become important in mid-infrared spectroscopy [8]. The development of traditional lasers emitting in the mid-infrared region has been challenging, although presently, laser technology is also extending towards longer wavelength regions in the form of quantum cascade and interband cascade lasers [9, 10]. The mid-infrared region is loosely defined, but it is often considered to cover the wavelength region starting from about 3 µm and extending to a few tens of µm. The mid-infrared region is important to molecular spectroscopy, because the fundamental vibrational transitions lie in this region. The fundamental transitions, where only one vibrational quantum is excited, are often up to two orders of magnitude stronger than overtone or combination transitions. As a result, the mid-infrared region often offers better sensitivity. In this thesis, various OPO light sources are used to take advantage of the strong mid-infrared transitions.

A recent example of a novel light source, which has been gathering vast interest, is the optical frequency comb (OFC) [11]. An OFC is a laser source, which emits thousands of laser lines over a broad wavelength region. Frequency combs can be used directly as light sources [12], where they combine the coherent properties and the high brightness of a laser, with an exceptionally wide optical spectrum. With an OFC, a wide spectrum can be recorded simultaneously, while with a typical single mode laser, wavelength tuning is required to record a spectrum. Furthermore, an OFC often has exceptionally good wavelength stability. They can be used to accurately measure or to stabilize the wavelength of a single mode laser, allowing a transition line position to be recorded with high precision and accuracy. [13, 14].

In this thesis, highly sensitive spectroscopic techniques are used to detect previously unobserved spectral features. CRDS was used to detect double resonance transitions of acetylene (C_2H_2). Acetylene is widely used in high-resolution spectroscopy as a model compound [15, 16]. It has a linear symmetric structure, which gives rise to a regular and easily assignable infrared spectrum. However, this four atom molecule exhibits interesting intramolecular dynamics, which affects the detailed structure of its spectrum. Due to such effects, characteristic of polyatomic molecules, acetylene is also a useful prototype molecule for understanding properties of larger molecules [16]. Acetylene has an important role in many chemical systems. It is involved in flame chemistry [17], and the formation of polyaromatic hydrocarbons [18] and soot [19]. Acetylene is found in Earth's atmosphere, emitted almost exclusively by anthropogenic sources [20]. It has been detected in various astrochemical environments [21] and thought to contribute to the formation of carbon dust [22]. In this thesis, double resonance spectroscopy was used to access C_2H_2 transitions, which are absent in normal infrared spectra. An OFC was used in combination with the double resonance CRDS detection system, to reach a high wavelength accuracy and a sensitivity surpassing previous setups used to measure similar transitions.

Photoacoustic spectroscopy was used in this thesis for direct frequency comb detection of a radiocarbon isotopologue of methane ($^{14}CH_4$). This work produced the first reported infrared spectrum of $^{14}CH_4$. Methane is an important gas in energy production, since it is the main component in natural gas. It is also a powerful greenhouse gas. The best known application of radiocarbon measurements is carbon dating. When a deceased organism stops exchanging gases with its environment, its ^{14}C concentration diminishes over time by radioactive decay. The age of an organic sample

can thus be estimated from the ratio of ^{14}C and ^{12}C concentrations. For the same reason, the $^{14}C/^{12}C$-ratio can be used to differentiate between biogenic and fossil sources of carbon compounds. In the context of methane, this can be used to determine the biofraction of fuels mixed from biogas and natural gas [23]. It can also be used to differentiate between biogenic and fossile emissions [24] and to track the release of ^{14}C depleted methane from permafrost [25]. The radioactive $^{14}CH_4$ isotopologue is also known to be emitted by light water nuclear reactors [26]. Traditional detection methods of $^{14}CH_4$ require long measurement times or large and expensive facilities to operate. Development of spectroscopic analyzers could lead to cheaper and more compact field-deployable alternatives.

The rest of this thesis consists of four parts. Chapter 2 describes the basic rovibrational spectroscopy theory related to the measurements of this thesis. In chapter 3, the mid-infrared light sources used in the experimental setups are presented. Optical frequency combs are also introduced briefly, with the focus on generation of mid-infrared frequency combs. Chapter 4 outlines the spectroscopic detection methods used in the experimental setups. The direct absorption measurements of $^{14}CH_4$ are presented in the same chapter. Finally, chapter 5 introduces concepts from nonlinear spectroscopy required to comprehend the double resonance experiments. The results from the double resonance spectroscopy of C_2H_2 are also summarized.

Chapter 2

Rovibrational spectroscopy

The absorption of a photon of infrared radiation can excite a molecule to a higher energy vibrational state. A vibrational transition can be accompanied by a change in the rotational state of the molecule. The combined transition is referred to as a rovibrational transition. In this thesis, we will use the normal mode notation to refer to the vibrational states of the molecules [27]. For acetylene, the normal modes are the symmetric C-H stretching (ν_1), C-C stretching (ν_2), antisymmetric C-H stretching (ν_3), doubly degenerate symmetric bending (ν_4), and doubly degenerate antisymmetric bending (ν_5) vibrations. The degeneracy refers to the fact that there are multiple modes with the same normal mode frequency. The degenerate bending motions of acetylene can induce an angular momentum around the molecular axis, which is characterized by the vibrational angular momentum quantum numbers l_4 and l_5 [27]. Figure 2.1 shows a schematic picture of the acetylene normal modes. For methane, the normal modes can be characterized as the symmetric stretching (ν_1), doubly degenerate bending (ν_2), triply degenerate stretching (ν_3) and triply degenerate bending (ν_4) vibrations.

In the normal mode picture, a vibrational energy state is marked as a sum of normal mode vibrations. For example, the vibrational state of acetylene, where one quantum of the symmetric C-H stretching and two quanta of antisymmetric C-H stretching vibrations are excited, is marked as $\nu_1 + 2\nu_3$. For the states of acetylene, which involve

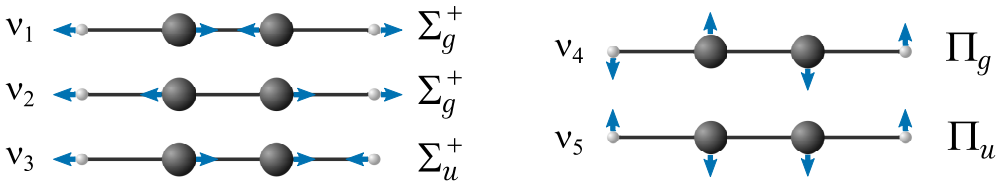

Figure 2.1: The normal modes of acetylene and their symmetry species [27]. The bond lengths, atom radii and the displacement vectors are not to scale. Both bending modes ν_4 and ν_5 are degenerate, because the vibration can take place in the plane of the paper as well as perpendicular to it. The degenerate bending vibrations can give rise to an angular momentum around the molecular axis.

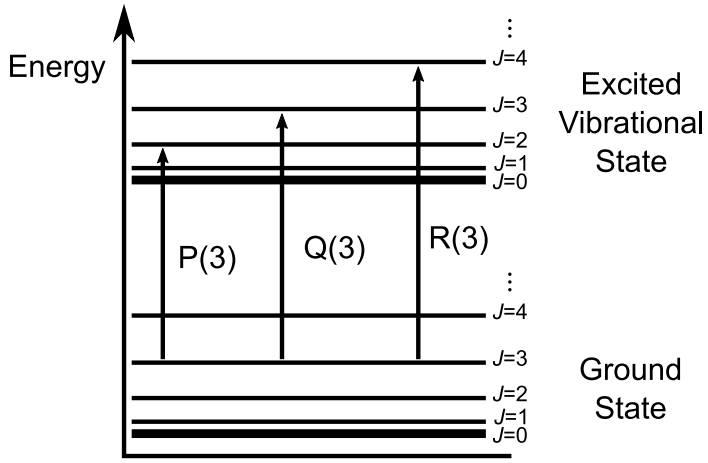

Figure 2.2: Schematic picture of a rovibrational energy diagram. The ground state and all the excited vibrational states include a set of rotational levels. Transition bands consist of narrow lines caused by the transitions between the rovibrational levels, which, for absorption, are represented by the upward arrows in the diagram. The change of the rotational quantum number J during the transition separates the lines into branches. The figure shows single transitions from P ($\Delta J = -1$), Q ($\Delta J = 0$) and R-branches ($\Delta J = +1$).

the bending quanta, the vibrational angular momentum quantum numbers are marked as superscripts above the corresponding vibration ($\nu_4^{l_4}$ and $\nu_5^{l_5}$). Each vibrational state has its own set of rotational energy levels. The rotational levels are also quantized and characterized by the rotational quantum number J. Figure 2.2 shows a schematic picture of a rovibrational energy diagram.

A rovibrational transition between two states can be excited by infrared radiation with an optical frequency (ν) matching the energy difference between the initial (E_1) and final (E_2) states:

$$\nu = \frac{E_2 - E_1}{h} \tag{2.1}$$

The nominator h is Planck constant, which acts here as a conversion factor between the units of frequency and energy. In spectroscopy, it is common to use wavenumbers, which are given by dividing the frequency by the speed of light c: $\tilde{\nu} = \nu/c$. For acetylene, the rovibrational energy has a simple form given by the equation:

$$\frac{E}{hc} = G + BJ(J+1) - DJ^2(J+1)^2 \tag{2.2}$$

The parameter G is the vibrational term value, B is a vibrational state specific rotational coefficient, and D is a centrifugal distortion coefficient. For a better description of the energy, more terms with higher orders of J can be added to the equation.

Not all transitions between rovibrational states can be excited by infrared light. The allowed transitions are given by so-called spectroscopic selection rules. For linear symmetric molecules, such as C_2H_2, the selection rules forbid transition between two symmetric vibrational states. The ground vibrational state is symmetric, with a term

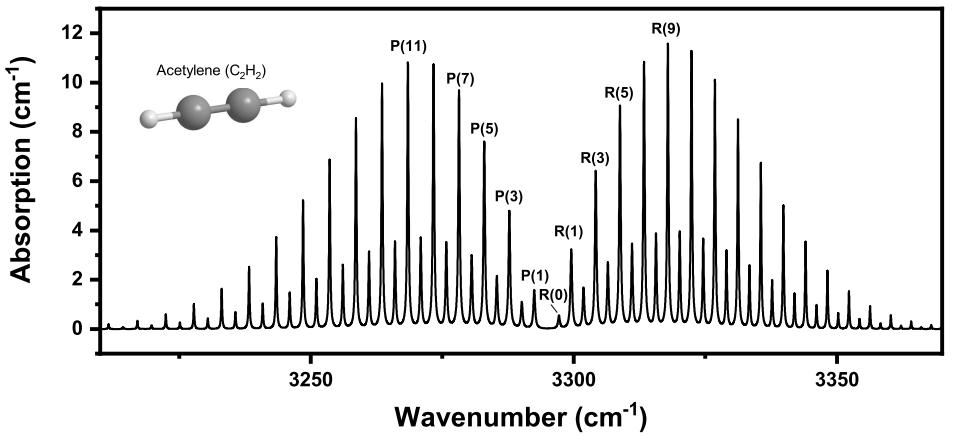

Figure 2.3: Spectrum of the ν_3 fundamental transition band of acetylene, simulated using data from the HITRAN database [28]. The simulatation was calculated for pure C_2H_2 at a pressure of 1 atm and temperature of 298 K, using *HITRAN on the web* [29].

symbol Σ_g^+. The symbol Σ refers to the vibrational angular momentum being zero, the superscript refers to the symmetry of the wavefunction in respect to a reflection along a plane containing the molecular axis, and the subscript refers to inversion symmetry, where g denotes a symmetric state and u an antisymmetric state. The vibrational states of acetylene considered in this work are all Σ^+ states. The allowed one-photon transition between such states are of the form: $\Sigma_g^+ \leftrightarrow \Sigma_u^+$ [27]. That is, only transition between states with different inversion symmetries are infrared active. The selection rules do not define the strengths of the transitions. Allowed transitions can be so weak that they are practically unobservable.

The selection rules for one-photon rovibrational transitions between Σ states of acetylene require that the rotational quantum number J changes by one [27]. A vibrational transition band of a $\Sigma_g^+ \leftrightarrow \Sigma_u^+$ transition is therefore divided into two branches: for R-branch, the change is $\Delta J = +1$ and for P-branch, the change is $\Delta J = -1$. The transitions of the R-branch are therefore excited by radiation of higher frequency, because the rotational energy increases in the transition. Combining these selection rules with equations 2.1 and 2.2 leads to a vibrational transition band structure of the form shown in figure 2.3, where the transition lines are separated by about $2B$ due to the rotational energy fine structure of the vibrational states. The lines are identified as $R(J'')$ or $P(J'')$, where J'' is the rotational quantum number for the lower state of the transition (figure 2.2).

The band structure of methane is more complicated. Figure 2.4 shows the band of the fundamental transition $\nu_3 \leftarrow$ GS, where GS refers to the vibrational ground state. The basic shape of the P and R-branch is similar to the case of acetylene, with approximately equidistant series of lines. There is additionally a series of overlapping transition lines between the P- and R-branches. This is the Q-branch with transitions of the form $\Delta J = 0$, which are also allowed in the fundamental ν_3 transition of

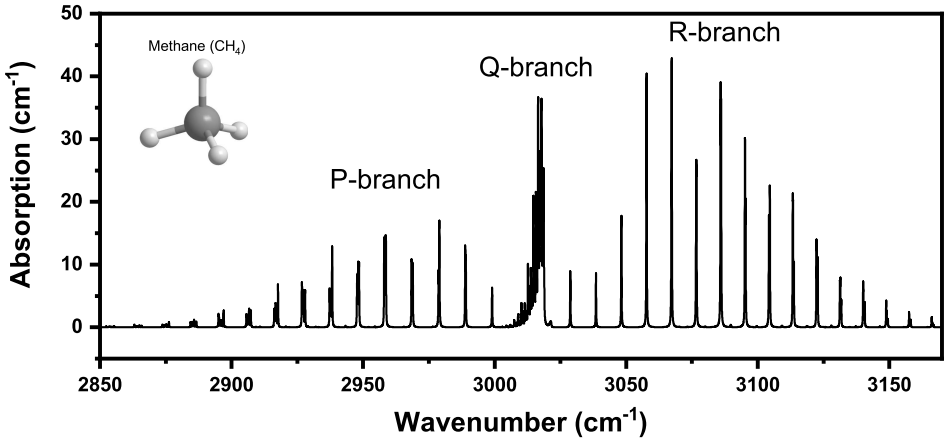

Figure 2.4: Spectrum of the ν_3 fundamental transition band of methane, simulated using data from the HITRAN database [28]. The simulatation was calculated for pure CH_4 at a pressure of 1 atm and temperature of 298 K, using *HITRAN on the web* [29].

methane. In addition, each line is split into a multiplet, because of the Coriolis interaction with different vibrational states [27]. The effect is more prominent for lines away from the band center, for which J'' is larger. The splitting is most apparent near the edge of the P-branch.

2.1 Transition line shape

The Beer-Lambert law describes the intensity of light as a function of travel distance, when it propagates through an absorbing sample:

$$I(\nu, l) = I_0(\nu)e^{-\sigma(\nu)Nl} \tag{2.3}$$

The decrease in the irradiance I at optical frequency ν, relative to the original input I_0, depends on the path length l through the sample, the attenuation cross section σ, and the number density of the absorbing species N. The cross section σ is a measure of the strength of any rovibrational transition at the wavelength of the input light.

For an isolated transition between two energy states, the shape of the $\sigma(\nu)$ frequency dependence is a sharp feature around a center transition frequency ν_0, matching the condition 2.1. The shape of the transition line depends on the measurement conditions. For a general case, we can write:

$$\sigma(\nu) = \sigma_0 g(\nu) \tag{2.4}$$

The function g decribes the shape of the line and its integral is normalized to 1, so that the integrated cross section is given by:

$$\sigma_0 = \int_{-\infty}^{\infty} \sigma(\nu)\mathrm{d}\nu \tag{2.5}$$

The lifetimes of the energy states involved in the transition imposes the lowest limit for the width (Γ) of the line. Lifetime broadening results in a Lorentzian line profile, given by [4]:

$$g(\nu) = \frac{1}{\pi} \frac{\Gamma}{(\nu_0 - \nu)^2 + \Gamma^2} \tag{2.6}$$

The linewidth Γ gives the half width at the half maximum, and is related to the lifetimes of the upper (τ_2) and lower (τ_1) states as [4]:

$$\Gamma = \frac{1}{2} \left(\frac{1}{2\pi\tau_1} + \frac{1}{2\pi\tau_2} \right) \tag{2.7}$$

The lifetime is ultimately limited by the decay through spontaneous emission. It is worth noting that using angular frequencies $\omega = 2\pi\nu$ simplifies some of the presented equations, for example the relation between the linewidth and the state lifetime. However, this thesis mostly uses optical frequencies, because they are commonly used in the experimental framework, and the linewidths are given in the same units.

Increasing pressure leads to a broadening of the linewidth of a transition, due to the higher rate of collisions between the molecules [30]. The collisions can be inelastic and cause energy state changes in the collision partners. This can be considered as a pressure dependent decrease in the state lifetimes, and a corresponding increase in the linewidth Γ. The inelastic collisions have a large impact on the linewidth in many molecules, where the majority of collisions can cause a state change, due to the abundance of close lying rotational energy levels. Collisions can also be elastic, where the internal state of the molecules remain unchanged. Elastic collisions can bring about phase changes during a radiative transition [30]. This causes additional pressure dependence in the linewidth Γ and it also leads to a small pressure dependent shift in the center frequency ν_0 in equation 2.6. The effect of both elastic and inelastic collisions introduces a linear pressure dependence to the linewidth Γ [30]. The magnitude of the pressure broadening and shift depends on the interactions between the collision partners so it is specific to the absorber and the surrounding gas mixture. The lifetime and pressure broadening can usually be considered homogeneous for all absorber molecules.

The Doppler effect causes line broadening, which becomes important at lower pressures. If the absorbing molecule has a nonzero velocity component along the optical axis (v_z), it senses the exciting wave as having a shifted frequency ν' according to:

$$\nu' = \nu + \frac{k}{2\pi} v_z \tag{2.8}$$

The quantity ν is the frequency of the light source in the laboratory coordinates. In the thermal equilibrium, the velocities of gas molecules are distributed according to the Maxwell distribution. When the frequency ν' matches the transition frequency ν_0 in the molecular coordinates, this looks like the molecule is absorbing at a shifted frequency in the laboratory coordinates. This leads to the Doppler broadened line shape of the transition around the center frequency ν_0. At the limit, where the Doppler broadening dominates over the homogeneous broadening, the line shape can be expressed as a normalized Gaussian function [31]:

$$g_D(\nu) = \sqrt{\frac{mc^2}{2\pi k_B T \nu_0^2}} \exp\left[-\frac{mc^2(\nu - \nu_0)^2}{2k_B T \nu_0^2} \right] \tag{2.9}$$

The parameter k_B is the Boltzmann constant. The half width at the half maximum is given by:

$$\Delta\nu_D = \sqrt{\frac{2k_BT\ln 2}{mc^2}}\nu_0 \tag{2.10}$$

The linewidth depends on the temperature T, the mass of the absorber m and the center frequency. The Doppler broadening is inhomogeneous, since the shift for an individual absorber depends on its velocity. For molecules with a particular velocity v_z, the line is further broadened according to the homogeneous broadening and to be accurate, the line shape should be considered as a convolution of the Gaussian and Lorentzian line shapes, which is called a Voigt profile.

Chapter 3

Mid-infrared laser sources

3.1 Optical parametric oscillator

An OPO produces laser like coherent light through nonlinear optical interaction, which can occur when high intensity coherent light is focused onto a material, which has a high nonlinear susceptibility. The polarization wave induced into such a material contains nonlinear terms, which are proportional to the increasing powers of the strength of the inducing electric field. Such terms become important when the intensity of the light is increased. Some of the nonlinear terms are oscillating with frequencies that differ from the frequency of the inducing light wave. The oscillating polarization field in turn radiates an oscillating optical field and owing to the nonlinear terms, the generated optical waves can have frequencies, which deviate from the frequency of the inducing light wave. Nonlinear optics has found valuable applications in transferring coherent light from the near-infrared wavelength region, where laser technology is well developed, into coherent mid-infrared radiation, where direct generation of laser light is more challenging. In this section, the basic principles of nonlinear optics are presented, focusing on the generation of mid-infrared light using an OPO.

When an electric field E is applied to a dielectric material, it induces a polarization density P [7]:

$$P = \epsilon_0 \chi^{(1)} E + \epsilon_0 \chi^{(2)} E^2 + \epsilon_0 \chi^{(3)} E^3 + ... \tag{3.1}$$

The first term given by $\epsilon_0 \chi^{(1)} E$, where $\chi^{(1)}$ is the linear susceptibility and ϵ_0 is the electric permittivity of free space, is referred to as the linear polarization. The quantities $\chi^{(n)}$, with $n \geq 2$, are referred to as the nth order nonlinear susceptibilities. The nonlinear susceptibilities are much smaller in magnitude than the linear one. In most cases, the linear response dominates the polarization of a dielectric medium, and the higher order terms can often be disregarded. However, when the electric field becomes strong, the nonlinear terms can become important. In general, P and E are vector quantities and $\chi^{(n)}$ is $n+1$'th rank tensor, which maps all the polarizations of the inducing light to the three coordinates of the material polarization wave, in reference to the geometry of the nonlinear material. For clarity of presentation, the quantities shall be treated as scalars. This corresponds to the inducing light possessing linear polarization and an effective nonlinear coefficient that maps that polarization to any one polarization of the induced wave.

The electric field of a monochromatic light wave is given by the sinusoidal formula:

$$E(r,t) = E_0 \cos(2\pi\nu t - kr + \phi), \tag{3.2}$$

where E_0 is the amplitude of the electric field, ν is its frequency, ϕ gives the initial phase of the wave, r is position, and t is time. The magnitude of the wavevector k is given by $k = n2\pi\nu/c$, where n is the refractive index of the medium. In an OPO, two such waves, which we shall refer to as pump (subindex p) and signal (subindex s) waves, are superimposed in the media. The total electric field is the sum of the two waves. The second order terms in 3.1 becomes:

$$P^{(2)} = \epsilon_0 \chi^{(2)} \left[E_\mathrm{p} \cos(2\pi\nu_\mathrm{p} t - k_\mathrm{p} r) + E_\mathrm{s} \cos(2\pi\nu_\mathrm{s} t - k_\mathrm{s} r + \phi)\right]^2 \tag{3.3}$$

Using trigonometric identities, this can be reformatted as:

$$\begin{aligned} P^{(2)} = \epsilon_0 \chi^{(2)} \Big\{ & E_\mathrm{p} E_\mathrm{s} + \frac{E_\mathrm{p}^2}{2} \cos(4\pi\nu_\mathrm{p} t - k_\mathrm{p} r) + \frac{E_\mathrm{s}^2}{2} \cos(4\pi\nu_\mathrm{s} t - k_\mathrm{s} r + \phi) \\ & + E_\mathrm{p} E_\mathrm{s} \cos\left[2\pi(\nu_\mathrm{p} + \nu_\mathrm{s})t - (k_\mathrm{p} + k_\mathrm{s})r + \phi\right] \\ & + E_\mathrm{p} E_\mathrm{s} \cos\left[2\pi(\nu_\mathrm{p} - \nu_\mathrm{s})t - (k_\mathrm{p} - k_\mathrm{s})r - \phi\right] \Big\} \end{aligned} \tag{3.4}$$

The nonoscillating first term corresponds to an effect called optical rectification. The two terms following it are the second harmonic generation (SHG) at both input frequencies. The last two terms are sum and difference frequency generation. It should be noted that for a medium with inversion symmetry, such as amorphous materials and centrosymmetric crystals, the second order susceptibility disappears [7]. To provide a simple picture of this constraint, for such a material, the inversion of the inducing electric field would lead to an inversion of the induced polarization. That is, changing the sign of the electric field should change the sign of the second order polarization. However, the power of two in equation 3.3 would null any change of the sign before the total electric field, i.e. the expression within the square brackets. Thus, the above inversion symmetry can only be followed if $\chi^{(2)}$ is zero. The nonlinear medium in an OPO is generally a noncentrosymmetric crystal. For all OPOs used in the experimental work of this thesis, the nonlinear material was lithium niobate.

The working principle of an OPO is based on the difference frequency generation, given by the last term in equation 3.4. The signal and idler waves generate a lower frequency wave called idler (figure 3.1). The polarization wave generating the idler is then of the form:

$$P^{(i)} = \chi_\mathrm{eff} E_\mathrm{p} E_\mathrm{s} \cos\left[(2\pi\nu_\mathrm{p} - 2\pi\nu_\mathrm{s})t - (k_\mathrm{p} - k_\mathrm{s})r\right] \tag{3.5}$$

The generated idler wave can be expressed as:

$$E = E_\mathrm{i} \cos(2\pi\nu_\mathrm{i} t - k_\mathrm{i} r) \tag{3.6}$$

Due to conservation of energy, the frequency of the idler wave is $\nu_\mathrm{i} = \nu_\mathrm{p} - \nu_\mathrm{s}$. For the difference frequency generation to be efficient, the polarization wave and the generated idler wave need to remain in phase throughout the medium [32]. This phase matching condition is satisfied perfectly when $k_\mathrm{i} = k_\mathrm{p} - k_\mathrm{s}$. However, k depends on the refractive index, which is a function of the wavelength. Therefore, the energy conservation

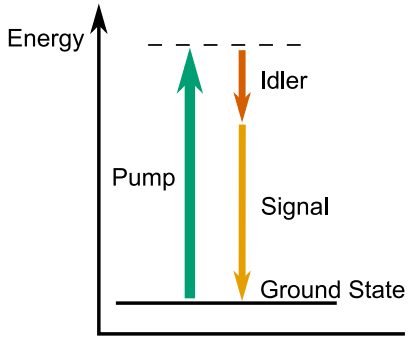

Figure 3.1: Energy diagram for the difference frequency generation involved in an optical parametric oscillator. A pump photon excites the nonlinear medium into a virtual state, which relaxes by emitting two lower energy photons. Of the emitted photons, the higher energy one is called the signal and the lower energy one is the idler.

and the phase matching are generally not satisfied simultaneously. There are various methods of fixing the phase matching problem. Currently, quasi phase matching (QPM) is the most used one [33]. The idler and polarization waves start to drift out of phase as a function of distance. After the so-called coherence length, the accumulated phase difference between the two waves starts to cause destructive interference. At that point, the polarization of the medium is flipped. This causes the polarization wave generated in the medium to change its sign, and consequently the interference between the two waves is again constructive [34]. The quasi phase matched medium is divided into periodic domains of opposite material polarization, according to the coherence length. The domain width is typically in the range of about 10–100 µm.

An OPO has typically only a high-power pump beam as input. When the pump power is high enough, it will spontaneously generate the signal and idler beams from initial power provided by quantum noise [35]. Because this effect can in principle happen at any pair of signal and idler wavelengths, its strength at any arbitrary wavelength pair is usually negligible. However, QPM is only efficient for a small range of signal and idler wavelengths. The range of wavelengths where the parametric amplification occurs in the QPM medium is set by the length of the QPM domains. Changing the poling period, for example by changing the temperature of the nonlinear medium to induce thermal expansion and a change in refractive indexes, can be used to tune the OPO output wavelength.

In an OPO, the nonlinear medium is placed inside of an optical cavity. The mirrors of the cavity are usually highly reflective for the signal beam. Any signal power generated by the spontaneous parametric generation propagates through the cavity back to the nonlinear medium and can act as an input for the difference frequency generation. The returning beam is further amplified by the pump power and simultaneously, more idler beam is generated. This imposes a threshold for the pump power: for the OPO to start oscillating, more signal power needs to be generated on a single pass through the nonlinear medium, than is lost to cavity losses. This configuration is called a singly resonant OPO (SRO). The idler beam is transmitted out of the cavity through one

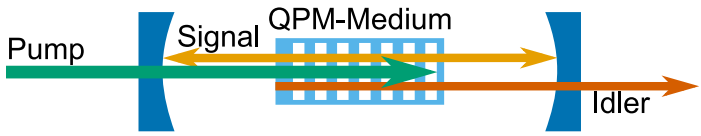

Figure 3.2: Singly resonant optical parametric oscillator. A quasi phase matched nonlinear crystal is placed in an optical cavity formed by two mirrors. An intense pump beam is sent through the crystal. The nonlinear interaction transforms power from the pump beam into the idler and signal beams. The signal beam starts oscillating within the cavity, while the idler beam is transmitted out.

of the mirrors. Alternatively, the cavity mirrors can reflect both the signal and the idler beams, resulting in a doubly resonant OPO (DRO). Since both the signal and idler beams oscillate in the cavity and act as inputs for the parametric process, the pump threshold of a DRO is lower than an SRO. However, a DRO tends to be less stable, because the cavity needs to fulfill two resonance conditions simultaneously [36]. A notable exception to this instability is the doubly resonant synchronously pumped OPO, described later in section 3.3.1. Figure 3.2 shows a schematic picture of an SRO.

The wavelength of the pump beam is usually in the near-infrared region, where the generation of high-power laser light, up to output powers of tens of watts, is straightforward. To generate a long wavelength idler beam, the signal wavelength is also usually in the near-infrared region. One typical configuration uses a pump wavelength around 1 µm and an OPO cavity designed for a signal wavelength of about 1.5 µm. The generated idler wavelength would be at about 3 µm, which corresponds to the fundamental C-H stretching region. In this thesis work, I have used an OPO pumped with a titanium-sapphire ring laser, working at the wavelength 800 nm, to produce an idler around 3 µm. This configuration allows wide tuning of the idler wavelength by changing the wavelength of the pump laser [37].

3.2 Optical frequency combs

Optical frequency combs are laser sources with an output spectrum consisting of a series of equidistant laser lines [11]. In the time domain, this corresponds to a train of laser pulses with a constant repetition frequency f_{rep}. The repetition rate also gives the separation between the laser lines. The optical frequencies of comb lines are given by:

$$\nu_n = f_{\mathrm{ceo}} + n \times f_{\mathrm{rep}}, \qquad n \in \mathbb{Z}_+ \tag{3.7}$$

The constant frequency shift f_{ceo} is called carrier-envelope offset. The integer n is a running index for each comb line. Figure 3.3 shows a schematic picture of the frequency comb spectrum. The repetition rate f_{rep} is usually in the radio frequency range, between a few hundred MHz to a few GHz. The frequency combs used in this thesis had a repetition rate of 250 MHz. The optical spectrum of a frequency comb is typically in the infrared region, corresponding to optical frequencies of a few hundred THz. The integer n is thus in the range of some hundreds of thousands for all the comb lines. The offset frequency f_{ceo} gives the position of the imaginary first comb line, for which n is zero, although such a line is outside the gain bandwidth

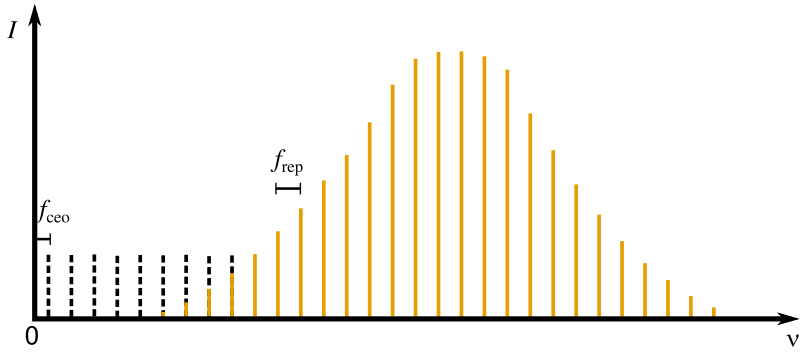

Figure 3.3: Schematic picture of the intensity spectrum of an optical frequency comb as a function of the optical frequency. The comb peaks are separated by a constant frequency f_{rep}. Each comb line is also shifted by an additional frequency f_{ceo}.

of any laser medium. The name carrier-envelope offset comes from the time domain picture, where it is related to a phase difference that accumulates between the pulse train envelope and the carrier wave phases over one laser cavity round trip, due to a difference between group and phase velocities. The bandwidth of a frequency comb varies a lot depending on the exact technology used to produce it, but a width of at least 100 nm is common. In the near-infrared region around 1550 nm, that width is about 12 THz in frequency units, which could contain tens of thousands of comb lines. The spectral bandwidth ($\Delta\nu$) is related to the width of the OFC pulses in the time domain, which is approximately given by $\delta t = 1/(2\pi\Delta\nu)$. With $\Delta\nu = 12$ THz, the pulse width is in the order of 10 fs

3.2.1 Mode locking

The production of a frequency comb laser requires the laser amplification to favor the generation of a train of short pulses over continuous-wave (CW) operation. An oscillation of short pulses with fixed pulse separation establishes a constant phase relation between the cavity modes. The process is referred to as mode locking.

The mode locking techniques can be divided into active and passive mode locking. Passive locking is usually achieved by introducing an element into the laser cavity, which modifies the cavity losses so that they depend on the intensity of the optical field. The classic example is a saturable absorber, for which the absorption loss decreases for higher irradiance [38]. For short pulses, the instantaneous power can become very high compared to CW light, so the saturation of the absorption loss favors the propagation of short pulses. Another widely used passive mode locking technique is known as Kerr-lens mode locking, which is also called self mode locking [39]. It is based on power dependence of the refractive index due to third order nonlinearity called the Kerr effect. The spatial power distribution within the laser beam profile causes the medium to act as a lens. Because the strength of the effect depends on the power, the cavity geometry can be designed so that it favors the propagation of the pulses, which are focused more due to the high instantaneous power. The Kerr effect also leads to intensity dependent self-phase modulation, which is utilized in the additive pulse mode

locking [40]. Two pulses from the laser are superimposed within the laser cavity and one of the pulses has encountered a Kerr-medium, so that its phase is altered by an intensity dependent shift. The laser system can be configured so that the interference of the pulses is most constructive where the peaks coincide, and the pulses start to drop more out of phase towards the edges of the pulse. Effectively, the interference amplifies the high intensity pulse center more than the pulse edges. This system can be implemented by splitting the laser pulses into two branches, one of which includes the Kerr-medium. Alternatively, the two branches can be different polarizations of the same cavity, in which case, the Kerr-effect can lead to mode locking through an intensity dependent polarization rotation [41].

Active mode locking refers to systems where the amplification or loss are actively varied to induce the pulsed operation. This can be achieved, for example, using cavity elements with losses that can be varied rapidly such as an acousto-optic modulator [42]. Alternatively, the pumping of the laser medium can be done in pulses, thereby modulating the laser gain. If the pumping repetition rate is synchronized to the cavity length, this can lead to mode locking [43]. In general, the passive mode locking methods lead to generation of shorter pulses, with pulse durations down to below ten femtoseconds [44], and larger spectral bandwidths.

3.2.2 Full stabilization

The optical frequency of all comb lines depends only on the two frequencies f_{rep} and f_{ceo}. If these frequencies are known, the absolute frequency of each comb line is known as well. Furthermore, if they are fixed to known constant values, the whole OFC spectrum is simultaneously stabilized.

The repetition rate is usually easy to measure with a fast photodiode, since it shows up as a strong peak in the radio spectrum of the OFC pulse train. The repetition rate can be tuned by changing the laser cavity length, because f_{rep} is equal to the inverse of the cavity round-trip time of the pulses. The carrier-envelope-offset is more complicated to measure, because it does not show up in the radiospectrum of the OFC output. The typically used method for measuring f_{ceo} is the f-to-$2f$ interferometry [45, 46] (figure 3.4). When the output of the OFC is frequency doubled using nonlinear optics, the comb peak ν_n produced its second harmonic at the frequency

$$2\nu_n = 2f_{\mathrm{ceo}} + 2n \times f_{\mathrm{rep}} \tag{3.8}$$

Assuming that the OFC spectrum is wide enough, it has a peak also at

$$\nu_{2n} = f_{\mathrm{ceo}} + 2n \times f_{\mathrm{rep}} \tag{3.9}$$

When the original OFC and its second harmonic are superimposed on a fast photodetector, they interfere and produce a signal that is beating with their difference frequency. This beat frequency can be measured and it has the value:

$$f_{\mathrm{beat}} = 2\nu_n - \nu_{2n} = f_{\mathrm{ceo}} \tag{3.10}$$

The method requires that the spectrum of the original comb spans over one octave, so that its higher frequency end will overlap with the second harmonic of the lower frequency end. Rarely, the width of the frequency comb output spectrum is over one

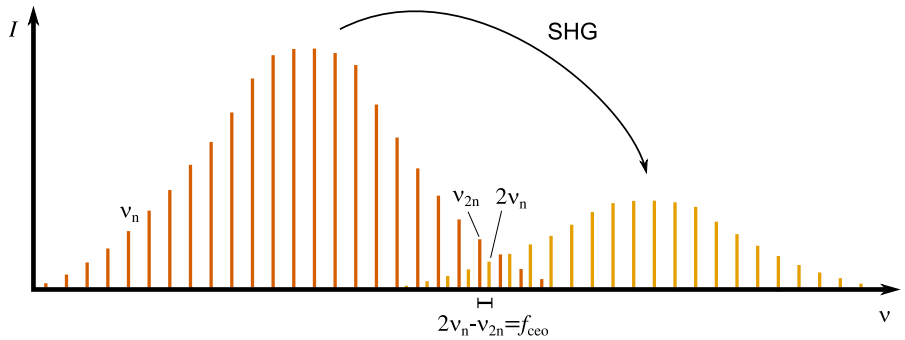

Figure 3.4: Principle of the f-to-$2f$ interferometry. The offset frequency f_{ceo} can be measured as the difference frequency between the original comb and its second harmonic. The difference frequency can be measured as the beat signal when the two combs are superimposed on a fast photodetector. This requires that the comb is wide enough to include at least some modes for which the integer n is two times that of a lower energy comb peak, i.e. there are observable modes with frequencies ν_n and ν_{2n}.

octave by itself, but usually this requires broadening the spectrum by, for example, sending the comb output through an optical fiber with strong optical nonlinearity [47, 48]. The offset can be tuned, for example, by changing the laser pump power [49].

The optical frequency of any of the OFC laser lines is a function of the two frequencies f_{rep} and f_{ceo}, which can be measured and fixed to constant values. Furthermore, since f_{rep} and f_{ceo} are radio frequencies, those constant values can be easily referenced to an atomic clock or the time standard distributed by the global positioning system [39]. An OFC can thus produce optical frequencies, which are traceable to the SI-second standard.

3.3 Mid-infrared frequency combs

Commercial optical frequency combs mostly operate in the near-infrared region. Typically they are based on the optical gain of titanium sapphire (wavelength around 800 nm) [45, 46], ytterbium (1 µm) [50], or erbium (1.5 µm) [51]. Thulium based OFCs, which operate at about 2 µm, are becoming common [52]. Frequency combs based on mid-infrared quantum cascade lasers are also being developed [53]. As an alternative to the development of mode-locked mid-infrared lasers, frequency combs can also be produced through nonlinear optical interaction. Third order nonlinear effects have been used to produce so called Kerr-combs in micro resonators [54] and cascaded second order nonlinear interaction has been used to produce mid-infrared frequency combs with a CW-OPO [55]. One widely used technique to transfer a near-infrared frequency comb into the mid-infrared region is to use the frequency comb as the pump beam for a synchronously pumped OPO (SPO). The mid-infrared combs used in this thesis work were exclusively SPOs, which are described in more detail in the following section. At present time, SPOs offer the best properties for high-resolution gas phase spectroscopy in terms of the width and stability of their optical spectra.

3.3.1 Synchronously pumped optical parametric oscillator

In an SPO, a near-infrared frequency comb, i.e. a mode locked near-infrared laser, is used as the OPO pump laser. The pump pulse generates signal and idler pulses within the nonlinear medium. After the signal pulse traverses the OPO cavity, it has to coincide with the next pump pulse in order for the parametric oscillation to proceed. The f_{rep} frequency of the pump comb is therefore directly transferred to the generated signal and idler pulse trains. However, this does not fix f_{ceo} of either of the generated comb structures. The sum of idler and signal f_{ceo} does become fixed relative to pump f_{ceo}, due to the conservation of energy. Therefore, if pump f_{ceo} is locked, it is enough to introduce one additional relation between the three offsets to stabilize the whole system [56]. The f_{ceo} frequency can be changed by tuning the SPO cavity length. This changes the signal comb spectral envelope, SPO power, and f_{ceo} simultaneously, while the pulse repetition rate is conserved, because the OPO will only work if the signal and pump pulses arrive at the nonlinear crystal at the same time [57].

A degenerate doubly resonant SPO is a special case that can be used to easily implement full stabilization of the comb structure [58]. It is referred to as half-harmonic generation (HHG). For HHG, the SPO is configured in a way where the idler and signal spectra overlap. The idler and signal combs become indistinguishable, as they share some of the same cavity modes, and therefore, f_{ceo} of the signal and idler combs become fixed as equals. There are, however, two different values that the SPO idler $f_{\mathrm{ceo,i}}$ can take relative to the pump $f_{\mathrm{ceo,p}}$:

$$f_{\mathrm{ceo,i}} = \frac{f_{\mathrm{ceo,p}}}{2} \vee f_{\mathrm{ceo,i}} = \frac{f_{\mathrm{ceo,p}} + f_{\mathrm{rep}}}{2} \tag{3.11}$$

Both values of $f_{\mathrm{ceo,i}}$ fulfill the conservation of energy and if the absolute value of the comb tooth frequencies are needed, $f_{\mathrm{ceo,i}}$ needs to be measured. Figure 3.5 shows the principle of an SPO and half harmonic generation.

The frequencies of the comb teeth produced by a degenerate SPO are stable since both f_{ceo} and f_{rep} are directly inherited from the pump comb. However, changes in the cavity length does induce changes in the SPO spectrum and power [59]. Because the OPO is doubly resonant, it will oscillate only within narrow cavity length ranges where both the signal and idler combs coincide with the OPO cavity modes [58]. Therefore, for long term operations, it is often beneficial to stabilize the cavity length. For example, a piezo actuator attached to one of the cavity mirrors can be tuned to produce a stable output power. A simple side of fringe locking can be used, but in that case, the output power cannot be locked to its highest value. The maximum power can be used with a dither lock, where the pump frequency or cavity length is modulated and the output power is measured with phase-sensitive detection [60]. However, the required modulation somewhat counteracts the inherent stability of the doubly resonant SPO. One option for a ditherless locking is to frequency double the SPO output and stabilize the second harmonic power instead [61]. Because SHG depends sensitively on the spectrum of the SPO and the phase-matching of the SHG crystal, the locking point can usually be chosen arbitrarily and close to the maximum of the SPO output power.

Stabilizing a singly resonant SPO is more involved. While f_{rep} remains the same as for the pump comb, and the energy conservation still requires that $f_{\mathrm{ceo,p}} = f_{\mathrm{ceo,s}} + f_{\mathrm{ceo,i}}$, the f_{ceo} frequency of the idler and signal combs can change relative to each

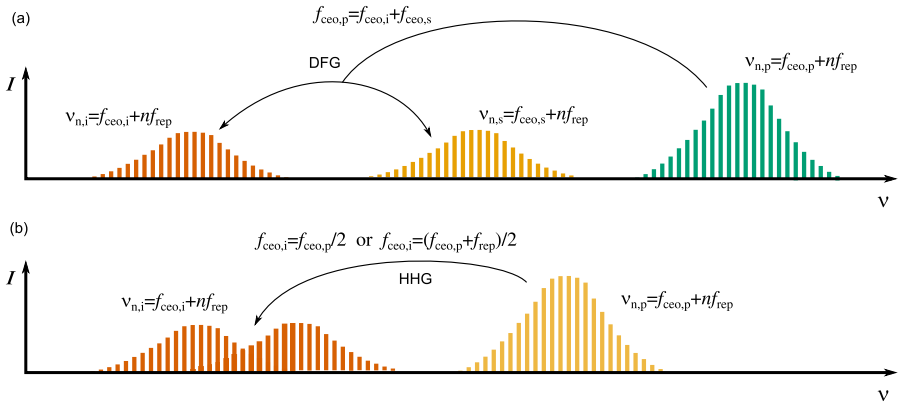

Figure 3.5: Principle of mid-infrared comb generation with synchronously pumped optical parametric oscillator and the relations governing the comb tooth frequencies. The pump comb (subindex p) is split into signal and idler combs through parametric conversion. In the general case (a), the offset frequencies of the signal and idler have to add up to the offset frequency of the pump due to conservation of energy. In half-harmonic generation (b), the signal and idler combs are partially degenerate, which additionally forces their offset frequencies to be equal.

other. If $f_{\mathrm{ceo,i}}$ needs to be stabilized, an additional locking loop is required. One way of achieving this is to use nonlinear frequency conversions to bring some harmonics or sum frequencies of the three combs involved in the SPO process to the same spectral region, and measure their beat frequency. The measured frequency can be used to establish another relation between $f_{\mathrm{ceo,p}}$, $f_{\mathrm{ceo,s}}$, and $f_{\mathrm{ceo,i}}$, which would stabilize the whole system [62]. In some cases, stabilizing the f_{ceo} frequency of the comb structure is not needed, particularly if the comb is not used for high accuracy frequency measurements. Even in that case, the cavity length often needs to be stabilized for long term usage, since changes in the length affect the the spectrum and output power of the SPO. With a singly resonant SPO, the output power is not a good locking parameter, because the power can be nearly unchanged over a wide range of cavity lengths near the optimal operation conditions [63]. The spectral envelop of either the signal or the idler comb provides a useful locking parameter. The SHG locking method should work with a singly resonant SPO as well, since the SHG efficiency strongly depends on the spectrum of the fundamental. Another option is to simply disperse part of the SPO output spectrum and measure the intensity at different wavelengths. The error function can then be produced, for example, by taking the difference between the intensities at two wavelengths [64], or using a position sensitive detector [63].

In this thesis work, a high-power singly resonant SPO was used for direct broadband spectroscopy of $^{14}CH_4$, which is described in section 4.2.2 and in article **V**. A degenerate doubly resonant SPO was used as a frequency locking reference in the nonlinear spectroscopy measurements described in chapter 5, and in articles **II** and **III**. The frequency locking scheme took advantage of the high stability, which the degenerate SPO inherits from the pump comb. The details of the SPO instruments can be found in the corresponding sections.

Chapter 4

Absorption spectroscopy methods

An absorption measurement can be made more sensitive by increasing the three parameters in the exponent in equation 2.3. A larger concentration of the absorbing species enhances the absorption. However, measuring the concentration is often the aim, and therefore, changing it may not be an option. Extending the path length is often implemented in various designs of the sample cell. The sample may be enclosed within a multipass cell or an optical cavity, where the light is reflected through the sample multiple times. The transition strength depends on the dipole moment function and the wave functions of the states involved in the transitions. Its precise value may be hard to predict. In rovibrational spectroscopy, a transition is generally stronger, when there are less changes in the vibrational quantum numbers. The fundamental transitions, which involve a change of only a single vibrational quantum, are usually much stronger than overtone or combination transitions. The development of spectroscopic techniques in the mid-infrared region is of interest, because many fundamental transitions reside there.

4.1 Cavity ring-down spectroscopy

In cavity ring-down spectroscopy (CRDS), the absorbing gas is enclosed inside an optical cavity consisting of highly reflective mirrors [2]. The optical power can be trapped between the mirrors, which effectively increases the absorption path length drastically. Laser light is shone into the cavity through one of the mirrors. In general, because the mirror reflectivity is high, little light is transmitted into the cavity. However, if the wavelength of the light fulfills the resonance condition of the cavity, the intracavity field and the light transmitting into the cavity interfere constructively, and consequently the power inside the cavity builds up. The resonance condition for the standing wave inside a linear cavity is given by:

$$n\lambda = 2l, \qquad n \in \mathbb{Z}_+ \tag{4.1}$$

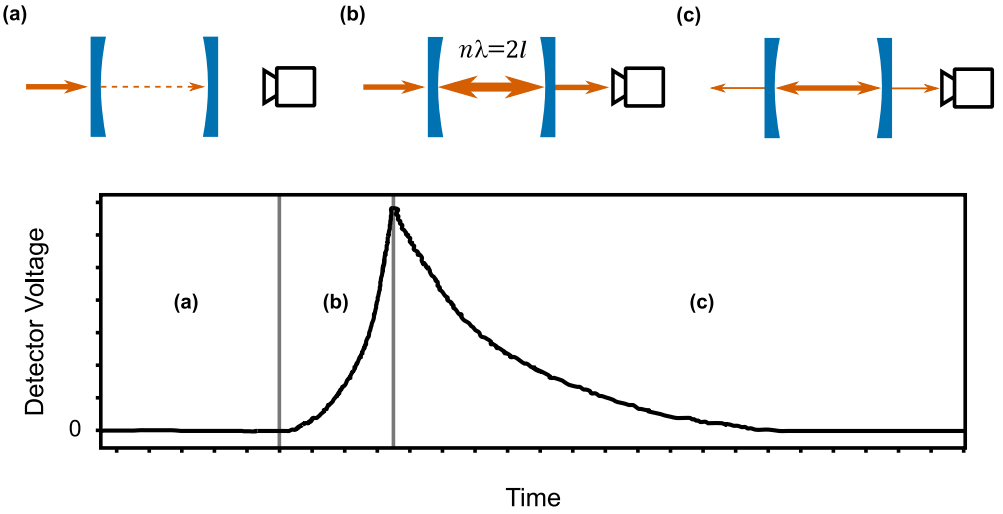

Figure 4.1: Principle of the CRDS measurement cycle. (a) In the general case, almost no light reaches the detector through the two highly reflective mirrors. (b) When the wavelength of the light source and the cavity length are brought into resonance, the intracavity optical power starts to build up. With optimal coupling, the optical power reaching the detector is of the same order of magnitude as the power incident on the cavity front mirror, but in practice it is often much less. (c) When the input light is shut off, the intracavity field starts to decay exponentially through the two cavity mirrors.

That is, the cavity length l has to be an integer multiple of half of the wavelength λ of the light. The resonance often needs to be brought about by tuning either the cavity length or the laser wavelength.

In CRDS, instead of measuring the absorption loss directly, the decay time of the intracavity field is recorded. The cavity power leaking out of the cavity through one of the mirrors (I_{out}) is detected. When the light input into the cavity ceases quickly enough, the output power decays exponentially according to:

$$I_{\text{out}} = I_{0,\text{out}} e^{-t/\tau_{\text{RD}}} = I_{0,\text{out}} e^{-k_{\text{RD}} t} \tag{4.2}$$

The time constant of the decay, τ_{RD} is often referred to as the ring-down time and k_{RD} as the ring-down rate. Figure 4.1 shows the principle of the CRDS measurement cycle.

A major advantage with CRDS is that the recorded signal has no dependence on power of the light source and thus, the method is mostly immune to laser power noise. The ring-down time is given by [65]:

$$\tau_{\text{RD}} = \frac{n}{c} \frac{l}{1 - R + L} \tag{4.3}$$

The variable R is the reflectivity of the cavity mirrors, which are assumed here to be identical, and L takes into account additional losses inside the cavity. For example,

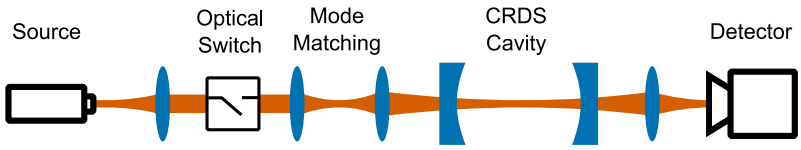

Figure 4.2: Principal components of a CW-CRDS measurement. The beam from a laser source is sent through a component that can act as a fast optical switch. An AOM is often used, but the switch can sometimes be even omitted completely, if the switching can be done directly with the laser source. Mode matching optics are needed to match the transverse spatial pattern of the laser beam to the transverse mode of the CRDS cavity. The cavity output is focused onto a fast photodetector.

loss due to an absorbing gas is of the form $L = \sigma N l$. As an example, a lossless 1 m cavity, with mirror reflectivity of 0.9999 corresponds to a ring-down time of 33 µs. This is also the mean lifetime of photons inside the cavity, so the mean distance travelled by the photons inside the cavity is 10 km.

An absorption spectrum can be recorded by measuring the ring-down time as a function of the wavelength of the light source. Assuming that the L is caused solely by the absorbing gas, its absorption can be calculated as:

$$\sigma N = \frac{n}{c}\left(\frac{1}{\tau_{\mathrm{RD}}} - \frac{c}{n}\frac{1-R}{l}\right) = \frac{n}{c}\left(\frac{1}{\tau_{\mathrm{RD}}} - \frac{1}{\tau_0}\right) = \frac{n}{c}(k_{\mathrm{RD}} - k_0) \tag{4.4}$$

It is often useful to give the absorption relative to an empty cavity ring-down time (τ_0) or rate (k_0). These are the corresponding decay parameters for the same cavity without the absorbing gas. Usually, τ_0 is not measured separately, but it is treated as the background level of the measurement.

The CRDS method was initially introduced for pulsed lasers [2], where the light source turning off happens naturally. However, using CW lasers has proven advantageous. They allow for detection of the ring-down decay with a high signal-to-noise ratio and high wavelength resolution [65]. They also avoid possible issues arising from exciting multiple cavity modes simultaneously [66]. However, the coupling between the cavity and the CW light source needs to be terminated at a time scale well below the cavity ring-down time. This is often done by using an external device that acts as an optical switch, such as an acousto-optic modulator (AOM) [65]. Techniques with no external switches have also been demonstrated, where the decoupling of the resonance between the laser and the cavity can be done, for example, by tuning the cavity length [67], tuning the laser frequency [68], or switching off the laser drive current [69]. Figure 4.2 shows a schematic example of a CRDS setup with a CW laser source. In articles **I**, **III**, and **IV**, CRDS is used to measure weak two-photon transitions.

The most sensitive CRDS setups rely on long averaging times to reach the lowest detection limits. One of the important parameters with CRDS is therefore the long-term stability of the measurement. As mentioned above, empty cavity τ_0 is often assumed to be constant and simply subtracted from the measured spectrum. However, during long time scales, τ_0 is known to vary slowly over time. Such changes may originate from, for example, changes in the environmental condition such as surrounding temperature or pressure, or small alignment changes due to mechanical instability [70].

Environmental changes can couple into the ring-down time through residual etalon effects with other optics in the measurement setup [71]. There are many advanced CRDS setups, which attempt to counteract the limitation caused by the drifting τ_0 level. If τ_{RD} is periodically measured at two wavelengths, one of which has no measurable absorption, it can be used to subtract the drifts in τ_0 [70]. Measuring the CRDS spectrum quickly and averaging the complete spectra, instead of averaging τ_{RD} at each point, has been shown to lead to long stable averaging times [72]. Saturated absorption CRDS uses saturation of the measured absorption line so that the relative contributions of the absorption and τ_0 to the total measured τ_{RD} changes throughout the ring-down decay [73]. Both contributions can thus be extracted from a single ring-down decay using a more complicated fitting function than a single exponential model. Taking the difference between two uncorrelated ring-down times, or using a more complicated fitting function increases the uncertainty of the measurement on short time scales [70, 74]. However, this limitation is often surpassed by the ability to use a longer averaging time to reach an overall better performance. Later in this thesis, section 5.2.2 introduces a novel method of rapid background subtraction when measuring double resonance transitions with CRDS.

4.2 Photoacoustic spectroscopy

Photoacoustic spectroscopy (PAS) is another highly sensitive absorption spectroscopy detection method. It has long been used for sensitive gas spectroscopy and trace gas analysis, especially since the invention of lasers [3, 75]. When molecules absorb light, they become excited and are transferred into higher energy states. An excited state has a finite lifetime, and consequently, the molecule quickly relaxes back to the ground state. The energy released during the transition back to the ground state is usually transferred to either photons, via spontaneous emission, or into kinetic energy as translational motion. The local increase in kinetic energy causes the gas to expand and sends out a pulse of pressure into the surrounding gas. When the absorption is modulated, for example, by tuning the wavelength or power of the light source, a periodic pulse train can be generated. A periodic train of pressure pulses is in principle a sound wave, which can be recorded with a microphone.

The pressure wave is generated only if the sample absorbs the incident light, and its amplitude depends on the strength of the absorption. The recorded electronic photoacoustic signal S_{PAS} can be described with the relation [76]:

$$S_{\mathrm{PAS}} = S_m C_c P N \sigma \tag{4.5}$$

The factors S_m and C_c are the microphone sensitivity and cell response constant, which together describe how well the absorbed power transfers into the output signal of the microphone. The remaining terms are the power of the light source P, the number density of the absorbing species N and the absorption cross section σ. One major advantage of the method is that it does not measure the change in intensity relative to its initial value. Instead, the generated signal is directly proportional to the incident power. The sensitivity of the method therefore improves with increasing optical power. Another advantage of PAS is that it works well with limited sample volumes. The cell response C_c depends in a complicated way on the geometry of the PAS cell, but generally it is inversely proportional to the volume [77].

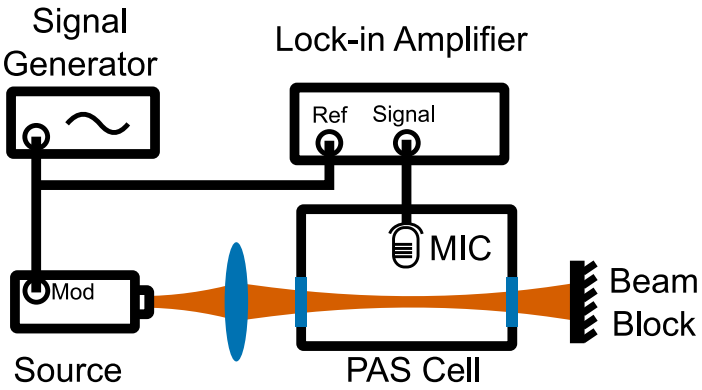

Figure 4.3: Schematic picture of a simple PAS setup. A laser beam is focused to a PAS cell through a transparent window. A sample gas inside the cell absorbs some of the laser power, which causes local heating along the beam path. The laser power or wavelength is modulated to produce an acoustic wave inside the cell. The wave is recorded with a microphone and the output is send to a phase sensitive detector with the modulating signal as the reference.

The modulation required to produce the pressure pulse train can be generated by changing the power or wavelength of the laser source. Wavelength modulation is converted to modulation of the absorbed power by the shape of the absorption line. Most early PAS setups used power modulation, often by chopping the light beam before the sample cell. However, wavelength modulation has usually been found to lead to better results [78]. For example, the PAS cell windows and walls may absorb some of the incident light, resulting in a broadband photoacoustic background signal. Since this is expected to be mostly independent of the wavelength, it is not picked up when using wavelength modulation. The microphone output is measured with phase sensitive detection, using the modulating signal as reference. Figure 4.3 shows an example of a common PAS measurement setup.

The developement of PAS has taken perhaps its largest steps in the improvements of microphone technologies. In the traditional PAS setups, the detectors were often diaphragm microphones, which lacked sensitivity. Two sensitive detectors have become common in modern PAS measurement setups: A quartz tuning fork (QTF) [79] and a cantilever microphone [80]. In the QTF enhanced PAS (QEPAS), the acoustic wave is generated at the resonance frequency of a QTF. Due to its high Q-factor, the movement induced in the QTF at the resonance frequency can be detected with high sensitivity via its piezo electric properties. In the cantilever-enhanced PAS (CEPAS), the diaphragm microphone is replaced with a small cantilever, with typical dimensions of a few mm in length and width and less than 10 µm in thickness. A cantilever is fixed in place only at one side and can move more freely. The movement does not involve stretching of the material, like in a diaphragm microphone. As a result, the acoustic wave can cause orders of magnitude larger movement in the cantilever and it has a wider linear range. The measurements described in section 4.2.2 make use of a CEPAS detector.

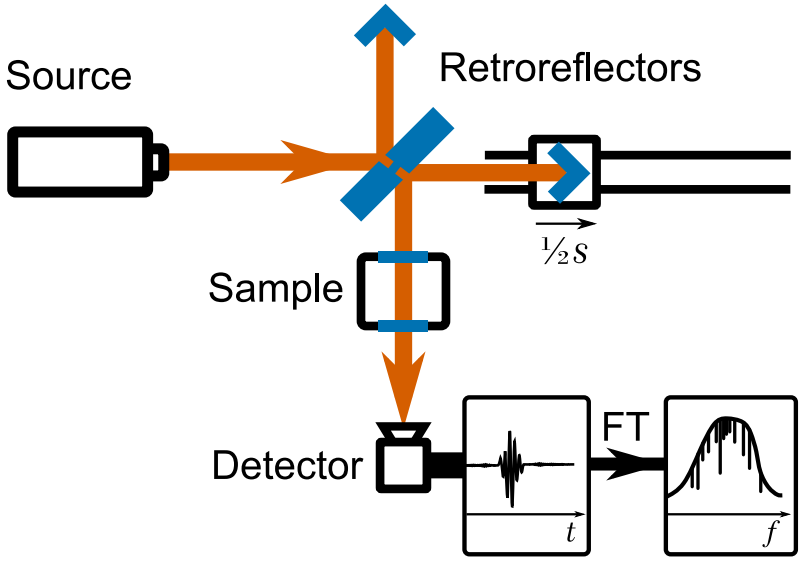

Figure 4.4: Schematic picture of a Fourier transform spectrometer. Light from the light source is split into two branches with a beam splitter. Both branches are reflected back with retroreflectors. The beams are superimposed again at a photodetector. One of the retroreflcetors is attached to a movable platform. As the platform is moved, the photodetector records an interferogram of the incident light. A Fourier transform of the interferogram gives the spectrum of the light reaching the detector. The spectrum shows the absorption peaks of any sample placed at the path of the light beam. The retroreflector is moved at half of the speed s, as defined in the text, because the optical path difference between the branches is twice the mechanical path difference.

4.2.1 Fourier-transform photoacoustic spectroscopy

Fourier transform spectroscopy is a well known method of dispersing a broadband light source into its wavelength components [81, 82]. Figure 4.4 shows a schematic picture of a Fourier transform spectrometer (FTS) based on a Michelson interferometer. The light is split into two branches, then superimposed again and sent to a detector. The relative length of the two branches is varied, for example by a moving mirror in one branch, to induce a changing phase shift between the light traversing the two branches. A phase shift (δ) causes the light from the two branches to interfere according to:

$$I(\lambda) = 2I_0(\lambda) + I_0(\lambda)\cos\delta \tag{4.6}$$

We have assumed for simplicity that the two branches have equal intensities (I_0). The phase shift, as a function of the path difference (d) is given by:

$$\delta = \frac{2\pi}{\lambda} \times d \tag{4.7}$$

Thus, the path difference induces a phase shift that is relative to the wavelength of the light. When the path difference is changing linearly with a speed (s), the interference

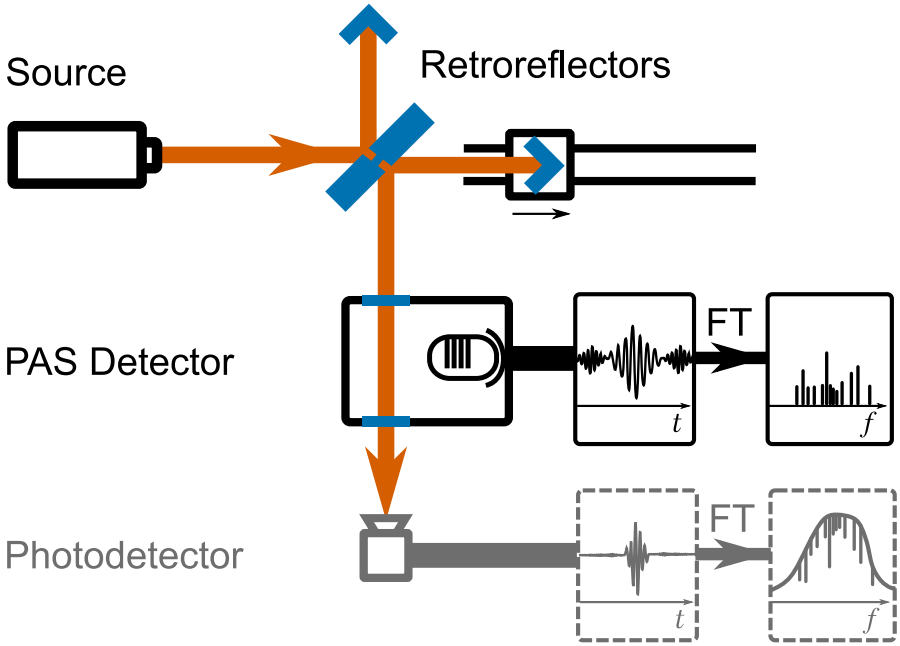

Figure 4.5: Schematic picture of a photoacoustic FTS. The traditional setup with a photodetector is shown in gray for comparison. The interference produces the modulation required to generate the photoacoustic signal. The interferogram produced by the microphone contains only the frequencies corresponding to the absorbing wavelengths. Similarly, the Fourier transform spectrum shows the absorption peaks, rather than the power spectrum of the light passing through the sample, like with the traditional FTS.

is oscillating according to:

$$I(\lambda) = 2I_0(\lambda) + I_0(\lambda)\cos\left(2\pi\frac{s}{\lambda}t\right) \tag{4.8}$$

That is, the light at the wavelength λ, produces an oscillating signal with a wavelength dependent frequency s/λ and an amplitude proportional to its intensity. When the light source is not monochromatic, the interference between the oscillations at different frequencies produces an interferogram, and the spectrum of the light source can be calculated as a Fourier transform of the interferogram. The resolution of the spectrum generated by the Fourier transform depends on the maximum path difference reached during the measurement.

In the context of PAS, the interference, as given by equation 4.8, acts as intensity modulation to produce the photoacoustic signal. Thus, an acoustic wave of the frequency s/λ is produced at all the wavelengths where the sample is absorbing [83]. Since the frequencies of the generated acoustic waves depend on the wavelength of the inducing light, an interferogram is produced in the microphone output signal. Figure 4.5 shows a schematic picture of a photoacoustic FTS. Measurements with a photoacoustic FTS have been demonstrated using thermal infrared sources [84], supercontinuum sources [85], and optical frequency combs [86]. When the recorded

spectrum consists of narrow lines and large areas of zero intensity, such as with PAS, where the interferogram has contribution only from the wavelengths that absorb light, the interferogram should be recorded symmetrically [87]. That is, the path difference needs to be scanned equal lengths on both sides of the zero path difference. With a symmetric interferogram, the power or magnitude spectrum can be calculated, which avoids problems arising from phase errors, at the cost of doubling the measurement time and causing nonlinearity in the noise [81].

4.2.2 Direct comb photoacoustic spectroscopy of $^{14}CH_4$

In article **V**, a broadband spectrum of radiocarbon methane ($^{14}CH_4$) was recorded using an FTS, with a CEPAS detector. Low ^{14}C concentrations are normally detected using scintillation counting or accelerator mass spectrometry (AMS) [88]. The latter one is usually considered the standard for measuring low ^{14}C concentrations. While AMS reaches very low detection limits below the modern natural abundance, the most sensitive measurements require large and complex facilities to operate. As an alternative, optical ^{14}C detectors, based on absorption spectroscopy, have been gaining interest [1, 89, 90, 91]. Optical detectors would be more affordable and compact in size, which could lead to the development of field operable ^{14}C detectors. So far, optical instruments have been limited to measurements of $^{14}CO_2$, but they have offered promising results. A sensitive saturated absorption CRDS laboratory setup has already reached similar detection limits as AMS [1]. For other compounds, a major limitation is the lack of spectral information. In article **V**, the first mid-infrared spectrum of $^{14}CH_4$ is published.

Due to the radioactivity of $^{14}CH_4$, its total amount in the measurement sample needs to be kept low. However, PAS is well suited for the measurement, since a small sample volume can be used and the sensitivity can be increased by using a high-power light source. In the article, a singly resonant SPO was used to produce a high-power mid-infrared frequency comb. I shall refer to this instrument as the singly resonant OPO comb (SROC). The SROC was pumped with a high-power ytterbium OFC, with maximum output power of 10 W and a center wavelength of 1040 nm. The nonlinear medium was a quasi-phase matched lithium niobate crystal, which was doped with magnesium oxide. The cavity was a four mirror bow tie configuration. The center wavelength of the signal and idler combs generated with the OPO were about 1550 and 3300 nm, respectively.

The offset frequencies of the SROC were not stabilized. Instead we used a simple locking scheme to stabilize the OPO cavity length and the idler spectrum envelope, similar to the scheme in Ref. [64]. Part of idler beam was sampled with a beam splitter and the sampled beam was dispersed with a grating. Two parts of the dispersed beam were focused on two photodetectors. The detector signals were sent to a differential amplifier. The difference of the intensity measurements at the two different wavelengths was then used as the error signal for a PID controller that tuned a piezo actuator attached to one of the cavity mirrors. The changes in the cavity length cause mostly monotonic changes in the idler center frequency, and the changes in the envelope are tracked by the difference signal, when the two intensities are measured at the opposite slopes of the comb spectrum. The mid-infrared power emitted by the SROC varied between about 0.4 and 1 W depending on the operating wavelength. In the

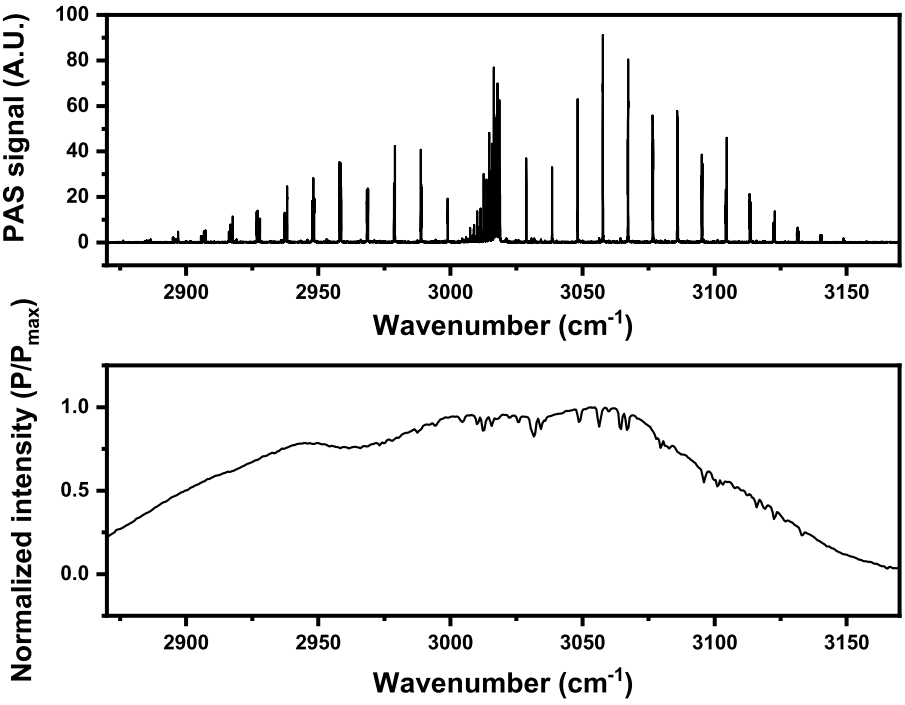

Figure 4.6: A raw photoacoustic spectrum of the $^{14}CH_4$ enriched methane sample, with SROC as the light source (upper). The lower figure shows a low-resolution spectrum of SROC. Note that the intense lines in the photoacoustic spectrum mostly belong to the main isotope $^{12}CH_4$, since it is the main component of the sample.

measurement, the center wavelength of the idler beam was set to about 3300 nm. The output power was about 500 mW. The width of the idler comb was about 150 cm^{-1}.

The photoacoustic spectrum was measured with an FTS (IFS 120-HR, Bruker), where a CEPAS cell (PA201, Gasera) filled with the sample gas was used as the detector. The electric bandwidth of the CEPAS detector was about 700 Hz, and therefore, a slow scanning speed s of 0.14 $cm\,s^{-1}$ was used. The wavelengths around 3300 nm thus have a frequency of about 420 Hz in the interferogram. The photoacoustic signal depends on the intensity of the light source (equation 4.5). Therefore, the PAS spectrum needs to be normalized by dividing it by the spectrum of the light source. The SROC spectrum was recorded with the same FTS and an HgCaTe semiconductor detector (PVI-2TE-5, VIGO). The light source spectrum was recorded with low resolution to avoid adding excess noise in the normalization, since only the spectral envelope is of interest here.

The $^{14}CH_4$ sample used in the measurements was diluted from a $^{14}CH_4$ enriched methane sample with nitrogen gas. The total methane concentration was about 100 ppm. The $^{14}CH_4$ concentration was about 1 ppm. Figure 4.6 shows the measured PAS spectrum, together with the spectrum of the SROC. The figure is an average

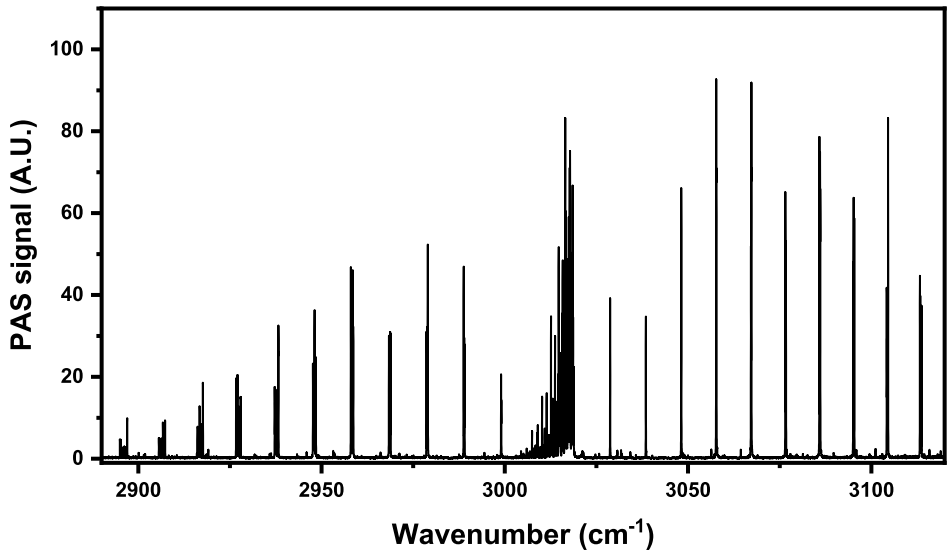

Figure 4.7: Photoacoustic spectrum of the $^{14}CH_4$ enriched methane sample divided by the light source spectrum. This eliminates the spectral dependence of the power in the photoacoustic signal, and consequently, the relative intensities of the lines correspond to the line strengths. The wavenumber axis is limited to the range where the light source spectral power is over half of its maximum. Near the edges of the SROC spectrum, the noise of the divided spectrum increases.

of three spectra, measured with a resolution of $0.02\,\mathrm{cm}^{-1}$. The PAS spectrum was divided by the normalized SROC spectrum, to produce the final absorption spectrum (figure 4.7). The main features of the spectrum are governed by the absorption of the anti-symmetric stretching vibrational (ν_3) band of $^{12}CH_4$. However, the spectrum also shows features that match the expected form of the ν_3 band of $^{14}CH_4$. The structure of the ν_3 band of both isotopologues are similar, except the lines of $^{14}CH_4$ are shifted by about $18\,\mathrm{cm}^{-1}$. Each line of the rotational structure is split into a multiplet of lines due to Coriolis interaction with other vibrational states. The component lines of a multiplet overlap due to pressure broadening and the splitting gives rise to a distinctive envelope shape of each multiplet. Because the isotope shift is small compared to the energy of the vibrational states, the Coriolis splitting is affected only slightly, and therefore, the shapes of the line multiplets between the isotopologues are similar [92]. The change in the mass of the center atom changes the rotational constant, and hence the separation between the line multiplets of the rotational structure, but this difference is also relatively small. In the article, we performed a simple band fit to the observed lines and the results for the band center and the rotational structure coefficient were 3000.62 and $10.08\,\mathrm{cm}^{-1}$, respectively. The corresponding parameters for the main isotopologue $^{12}CH_4$ are 3018.91 and $9.87\,\mathrm{cm}^{-1}$ [92]. To show the comparison between the ν_3 bands of the two isotopologues, figure 4.8 shows part of their R-branch spectra, side by side. The $^{14}CH_4$ spectrum is from the measurement, but

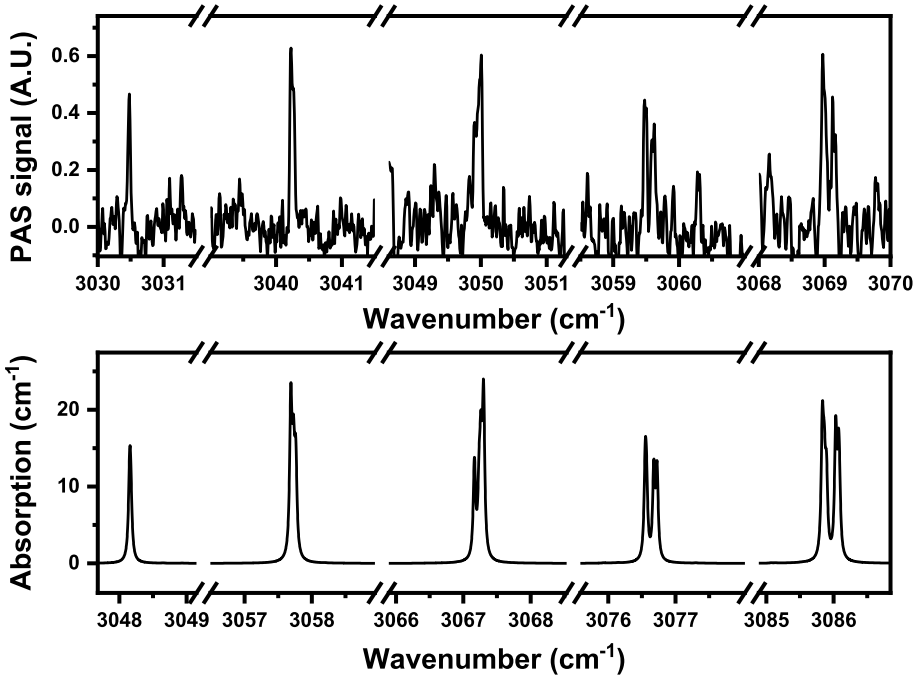

Figure 4.8: The strongest R-branch lines of the ν_3 band of $^{14}CH_4$ (upper). For comparison, the lower figure shows a HITRAN spectrum of $^{12}CH_4$ where the wavenumber axis has been realigned with respect to the upper figure, according to the changes caused by the change of the carbon isotope (see text). The figure shows the similarity of the two spectra in terms of the relative intensities and the shapes of the lines due to the Coriolis splitting.

nearby $^{12}CH_4$ and water lines have been fitted with line profiles and subtracted from the spectrum, to better isolate the unassigned lines. The $^{12}CH_4$ spectrum is from HITRAN data [28]. Its wavenumber axis ($\tilde{\nu}_{C12}$) has been aligned to the axis of the PAS spectrum ($\tilde{\nu}_{C14}$) according to:

$$\tilde{\nu}_{C12} = \frac{9.87\,\mathrm{cm}^{-1}}{10.08\,\mathrm{cm}^{-1}} \times (\tilde{\nu}_{C14} - 3000.62\,\mathrm{cm}^{-1}) + 3018.91\,\mathrm{cm}^{-1} \tag{4.9}$$

This approximately simulates the isotope shift and the change in the rotational constants, so that the lines of the two isotopologues coincide. The similarity between the spectra of the two isotopologues, in terms of the relative intensities between the lines and the line shapes caused by the Coriolis splitting, corroborate that the newly observed lines belong to $^{14}CH_4$. Figure 4.9 shows the Q-branch of the ν_3 band of $^{14}CH_4$. Because of the low SNR and the fact that the branch overlaps severely with the P(2) line of $^{12}CH_4$, no assignment could be performed with confidence. For reference, the clearest features near the beginning of the band are marked in the figure.

For the tallest $^{14}CH_4$ peak, at about $3040\,\mathrm{cm}^{-1}$, a single scan gives an SNR of

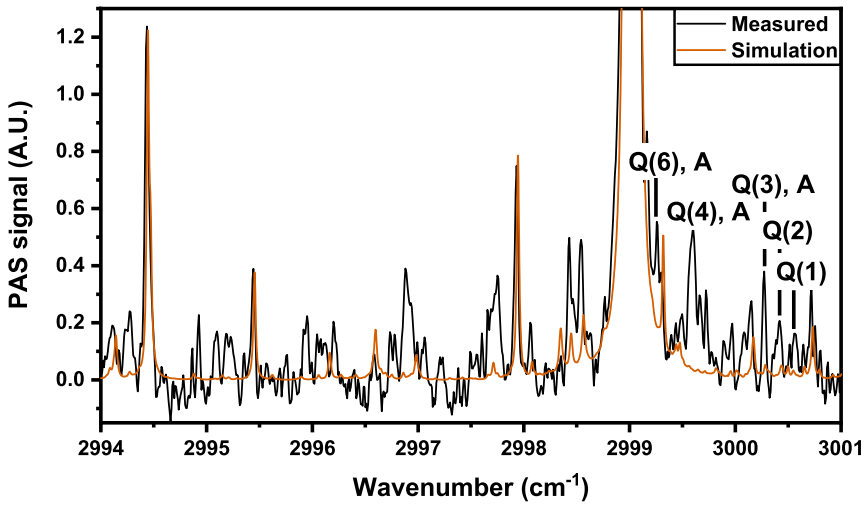

Figure 4.9: Q-branch of the ν_3 band of $^{14}CH_4$. The orange line is a simulated spectrum of $^{12}CH_4$ and water. Due to the low SNR and overlap with the P(2) line of $^{12}CH_4$, confident assignment could not be performed. The strongest and clearest features are marked in the spectrum for reference.

about 11. The SNR is defined here as the ratio between the height of the peak and one-standard deviation of the noise of a flat region near the foot of the peak. The $^{14}CH_4$ concentration in the sample was 1 ppm, so the noise equivalent detection limit is about 90 ppb. At the date of publishing, this was the lowest detection limit reported for a broadband PAS measurement. This result demonstrates the excellent scalability of the CEPAS detection when using a high-intensity light source.

The list of the lines extracted from the measured spectrum is reported in article **V**. The number of assignments is limited, due to the low SNR and because many of the P-branch lines overlap severely with the strong lines of $^{12}CH_4$. The spectra were calibrated according to the HITRAN line list of $^{12}CH_4$, which are known to high accuracy. The largest contributors to the wavenumber uncertainty of the reported lines are the low resolution of the measured spectra and the relatively low SNR. A simplified line profile was used for the fitting, which may also increase the uncertainty of the line centers. The line list is expected to be of assistance in the development of more sensitive optical $^{14}CH_4$ detectors, based on single mode lasers.

Chapter 5

Nonlinear spectroscopy

5.1 Saturation spectroscopy

In a more detailed description of absorption between two energy states (1 and 2), compared to the simple Beer-Lambert formula (equation 2.3), the strength of absorption is porportional to the population difference between the states [4]:

$$\alpha(\nu) = \sigma_{12}(\nu)(N_1 - N_2) \tag{5.1}$$

The population N_1 is for the lower energy state and N_2 is for the higher energy state. The state specific absorption cross section σ_{12} describes the transition strength between the states. In a thermal equilibrium, the state populations are proportional to the total concentration, and in the limit of weak absorption, where the absorption itself does not cause significant changes in the populations, the equation reduces to the Beer-Lambert law. The cross section prefactor is different, since it needs to account for the equilibrium population of the states.

When the population changes caused by the absorption are taken into account, the absorption coefficient gains an intensity dependence. While the functional form of the intensity dependent absorption coefficient varies according to the measurement conditions, the significance of this effect can be described using the saturation parameter (G), given by [93]:

$$G = \left(\frac{\mu_{12}E}{h}\right)^2 \left(\frac{2\pi\tau}{\Gamma}\right) \tag{5.2}$$

The dipole moment μ_{12} describes the strength of the transition moment between the specific states, E is the amplitude of the incident electric field, τ is the average decay time of the involved energy states, and Γ gives the homogeneous half width of the transition. Since E^2 is proportional to the intensity of the exciting light, the saturation parameter is often given as the ratio between the intensity and a saturation intensity (I_{sat}): $G = I/I_{\text{sat}}$. Saturation may become important when the intensity of the light and the magnitude of the transition moment are large. The state decay time decreases and transition width increases with pressure. As a results, saturation effects are more prominent at low pressures. The functional form of the saturated absorption coefficient depends on the measurement conditions. Below, the case of saturation of a Doppler broadened transition is described.

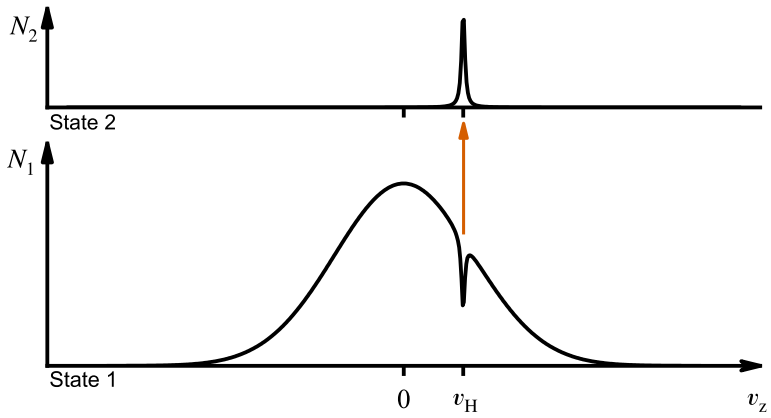

Figure 5.1: Schematic energy diagrams for two levels excited with a narrow linewidth laser. The contours show the population of the level as a function of molecular velocity along the optical axis. When the laser frequency is $\nu = \nu_0 + kv_H/2\pi$, a narrow velocity distribution from the lower state population is excited to the higher energy state. Because of this reduction in the population difference $(N_1 - N_2)$, the absorption coefficient depends on the laser intensity.

5.1.1 Hole burning

At low pressure, the Doppler effect dominates the width of an absorption line. Molecules moving with different velocities sense the incident light as having a frequency shifted according to the equation 2.8. When a single mode laser is used for the excitation, the laser linewidth is generally narrow compared to the Doppler width. As a result, the laser excites only a small distribution of velocities at a time, for which the resonance condition follows equation 2.8, with ν being the unshifted transition frequency (ν_0) and ν' the laser frequency. The width of the excited distribution (Γ_B) is proportional to the homogeneous width of the transition, but it is broadened according to the saturation parameter [94]:

$$\Gamma_B = \Gamma(1+G)^{\frac{1}{2}} \tag{5.3}$$

If the incident power is high enough, this results in a change in the population difference between the states and a perturbation of the Gaussian line shape. A narrow hole, often called the Bennett hole, appears in the population of the lower energy state. A corresponding peak of increased population accumulates on the higher energy state (figure 5.1). The saturating light cannot observe the hole itself when it is scanned over the Doppler line shape, but it will sense overall decreased absorption according to [93]:

$$\alpha(\nu) = \frac{\alpha(\nu)_0}{(1+G)^{\frac{1}{2}}} \tag{5.4}$$

The coefficient $\alpha(\nu)_0$ corresponds to absorption without saturation.

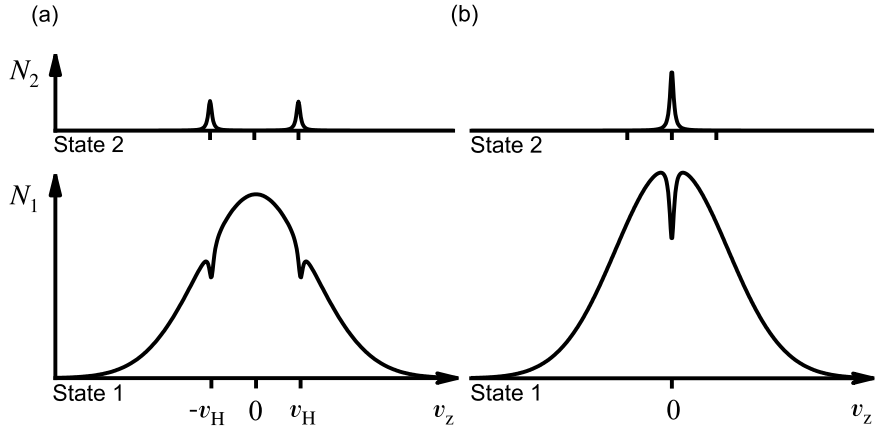

Figure 5.2: When the laser travels back and forth through the sample, the two counter propagating waves have the same frequency, but their wave vectors have opposite signs. The laser fulfils the resonance condition with two parts of the velocity distribution, since $kv_H = (-k) \times (-v_H)$. When the laser frequency is tuned to the line center, the counter propagating waves also sense the population change caused by the other wave, and the saturation is effectively doubled.

5.1.2 Lamb dip

When a laser beam is sent through a gas sample and then reflected back through it a second time, there are effectively two saturating waves that have opposite signed wave vectors. There are thus two sets of molecules that fulfil the resonance condition (equation 2.8), with opposite signed velocities. These appear in the Doppler line shape symmetrically on both sides of the line center. However, near the line center, the two Bennett holes start to overlap. This induces additional saturation and a narrow Lamb dip can be detected in the absorption at the line center when the laser wavelength is scanned over the Doppler profile [95, 96]. In the limit of weak saturation, the decrease in the absorption can be described with the formula [93]:

$$\alpha(\nu) = \alpha(\nu)_0 \left[1 - \frac{G}{2} \left(1 + \frac{\Gamma^2}{\Gamma^2 + (\nu - \nu_0)^2} \right) \right] \tag{5.5}$$

Far from the line center, the counter propagating waves saturate the absorption as individual waves and the reduction in the absorption is approximately equal to that given by equation 5.4. At the line center, the waves also encounter the saturation caused by the other wave, and the saturation parameter is effectively doubled for both waves (figure 5.2). The Lamb dip has a Lorentzian shape with a linewidth of the homogeneous width Γ. At low pressures, Γ can be orders of magnitude smaller than the Doppler width, and therefore, Lamb dip can be used to resolve the line center frequency ν_0 with high resolution.

5.1.3 Comb-assisted Lamb dip spectroscopy of CH_4

In article **II**, Lamb dip saturation spectroscopy was used as an example of an application of the OPO frequency comb system introduced in the article. The first direct locking between a CW-OPO and a mid-infrared OFC was established and a saturation spectroscopy measurement of methane was demonstrated with the OFC-locked CW-OPO.

The mid-infrared frequency comb was produced with a degenerate doubly resonant SPO. We shall refer to this mid-infrared OFC instrument as a doubly resonant OPO comb (DROC) for short. The DROC consisted of a six-mirror bow-tie cavity. The nonlinear medium was a 1 mm long periodically poled lithium niobate (PPLN) crystal. It was pumped with an amplified commercial Erbium OFC (FC1500-250-WG, Menlo Systems), with a center wavelength of 1560 nm and amplified output power of 400 mW. Both f_{rep} and f_{ceo} of the pump OFC were stabilized to a reference oscillator, which was referenced to a GPS time standard. As a result, f_{rep} and f_{ceo} of the DROC were also stable, since they are directly inherited from the pump comb (see section 3.3.1). The DROC cavity length was stabilized near the maximum output power with dither locking, by tuning the position of one cavity mirror with a piezo actuator. The maximum output power of the DROC was about 70 mW and the center wavelength was 3150 nm.

The CW-OPO was a singly resonant OPO consisting of a four mirror bow-tie cavity and a 5 cm long PPLN crystal as the nonlinear medium. The resonating signal beam wavelength was 1550 nm and the idler wavelength was about 3000 nm. The pump was a continuous-wave titanium sapphire ring-laser (MBR-PS, Coherent). The CW-OPO was singly resonant. The details of the titanium sapphire laser pumped CW-OPO are presented in reference [37]. The mid-infrared output from the CW-OPO was split into three branches with two CaF_2 plates. The transmitted beam, which contains most of the output power, was used for the Lamb dip measurement. The two reflections were used to stabilize the CW-OPO wavelength. One branch was used to stabilize the difference frequency between the CW-OPO and the DROC comb tooth nearest to CW-OPO wavelength. The CW-OPO and DROC beams were superimposed on a fast photodetector. A beat signal was observed between the CW-OPO and DROC and it was sent to a frequency-to-voltage converter circuit. The output from the circuit was input to an analog integrator circuit. The integrator output tuned the CW-OPO cavity length via a mirror attached to a piezo actuator. Locking the CW-OPO to DROC stabilizes its absolute wavelength, but there is still uncertainty about what that wavelength is. The beat signal alone does not reveal which comb tooth is nearest to the CW-OPO wavelength, and furthermore, the DROC f_{ceo} frequency can have two different values. To resolve these issues, the second reflection branch of the CW-OPO output was sent to a wavelength meter. As long as the accuracy of the wavelength meter is below half of f_{rep}, it is possible to resolve on which f_{ceo} value the DROC is operating and which is the nearest comb line. Then, a more accurate reading for the CW-OPO wavelength can be calculated from the comb formula 3.7 by adding or subtracting the measured beat frequency. Whether the CW-OPO wavelength is below or over the wavelength of the nearest comb tooth is apparent from to which direction the beat frequency moves when the CW-OPO wavelength is tuned slightly. The same locking method was also used in the frequency comb assisted double resonance measurements described in section 5.2.3.

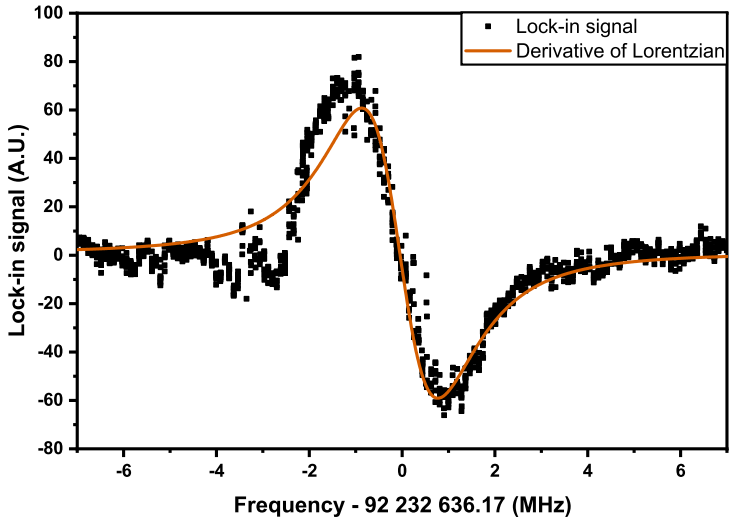

Figure 5.3: Lamb dip of the F_1 component of the R(5) line from the ν_3 band of CH_4. The line was excited with an OFC locked CW-OPO and measured with phase-coherent detection. There is an anomaly at the left edge of the line shape, which diverges from the expected model. This was likely due to residual amplitude modulation or wavelength dependent instability in the CW-OPO caused by the wavelength modulation.

The main CW-OPO output was sent through a 50 cm cuvette, which contained 30 mTorr of CH_4. The CW-OPO beam was reflected back through the sample onto a photodetector. The Lamb dip was measured with phase sensitive detection. The CW-OPO pump wavelength was modulated, and the photodetector signal was measured with a lock-in amplifier. The modulation frequency was 4.67 kHz, which was above the bandwidth of the locking circuit used to stabilize the CW-OPO wavelength. The sharp absorption features of the gas sample convert the wavelength modulation into amplitude modulation in the detector signal and the lock-in amplifier measures the strength of that modulation. The amplitude of the modulation is proportional to the derivative of the absorption line shape. The CW-OPO wavelength was scanned by tuning the repetition rate of the DROC pump comb, while the locking was established. Figure 5.3 shows the lock-in amplifier signal when the CW-OPO wavelength was scanned over the center of a CH_4 absorption line. The shape of the Lamb dip is Lorentzian and the form of the demodulated signal should be its first derivative. While the right-hand side follows the expected model well, the left-hand side is more irregular. This was most likely caused by either small wavelength dependent losses in the optical system, such as residual etalon effects, or sporadic instabilities of the CW-OPO power due to the modulation and locking. On a time scale of 1 s, the CW-OPO linewidth was about 1.5 MHz. This is significant relative to the width of the Lamb dip, which was about 4 MHz, and it may also have deformed the observed line shape. The measured line center frequency agreed with previous high-resolution measurements within about 1 MHz.

5.2 Double resonance spectroscopy

A one-directional saturating beam cannot detect the deformation of the Doppler profile by itself. However, if another probe beam is used to measure a transition, which shares the same lower state, it will sense the modified line shape. This is because the absorption of the probe beam depends on the population of the lower state (equation 5.1), which has been modified by the saturating beam. When the wavelength of the saturating beam is tuned to the side of the Doppler profile, and the wavelength of the probe beam is scanned over the whole transition line shape, the absorption of the probe beam decreases locally due to the depopulation caused by the saturating beam. Thus, in the absorption spectrum of the probe beam, the Bennett hole, burned by the saturating beam, appears in the Doppler profile [97]. Lamb dip spectroscopy is an example of this, with the reflection of the saturator acting as the probe beam, and the second transition is the same transition acted on by the saturator. In that case, the Bennett hole can be seen only at the line center, where the Doppler shifts coincided. On the other hand, if the probe beam is used to measure a transition that starts from the higher energy state of the saturated transition, it will sense the increased population pumped there by the saturating beam. In many cases, the higher energy state is practically unpopulated in thermal equilibrium, so the probe will sense only the narrow distribution excited by the saturating beam. Such double resonance transitions can be used for sub-Doppler measurements [98] and also to reach energy states, which are inactive in normal single photon transitions [99]. Figure 5.4 shows qualitatively typical probe spectra resulting from such double resonance transitions. If the probe beam wavelength is tuned to match a transition, which starts from the lower state of the saturated transition, the transition is termed a V-type double resonance. In a ladder-type double resonance, the probed transition starts from the higher energy state of the saturated transition, and leads to an even higher energy state. On the other hand, if the final state is of lower energy than the intermediate state, the transition is a Λ-type double resonance. The transitions measured in this thesis are ladder-type and therefore, they are the focus of the following discussion. Many of the results generally apply to all types of double resonance transitions, although there can be sign changes in the equations given below.

A sharp sub-Doppler feature excited by the saturating wave is Doppler shifted from the line center according to the wavelength of the saturating beam. The probe beam is interacting strongly only with the molecules with the same velocity component v_z. If the second transition occurs fast enough, so that in the intermediate state 2, the molecule has no interactions with other species, the transition frequencies are governed by a double resonance condition [97]:

$$\nu_{12} + \nu_{23} = \nu'_{\mathrm{S}} + \nu'_{\mathrm{P}} \,, \tag{5.6}$$

where $\nu'_{\mathrm{S}} = \nu_{\mathrm{S}} + k_{\mathrm{S}} v_z/2\pi$ and $\nu'_{\mathrm{P}} = \nu_{\mathrm{P}} + k_{\mathrm{P}} v_z/2\pi$ are the Doppler shifted frequencies of the saturating wave and probe wave, respectively. The condition states that in the molecular coordinates, the frequencies of the two exciting waves add up to the sum of the transition frequencies. The two transitions do not need to be individually in resonance. For a coherent two-photon transition, there does not have to be a state 2 near resonance with the saturating beam, but a resonance with a real intermediate state increases the strength of the two-photon transition by orders of magnitude [100].

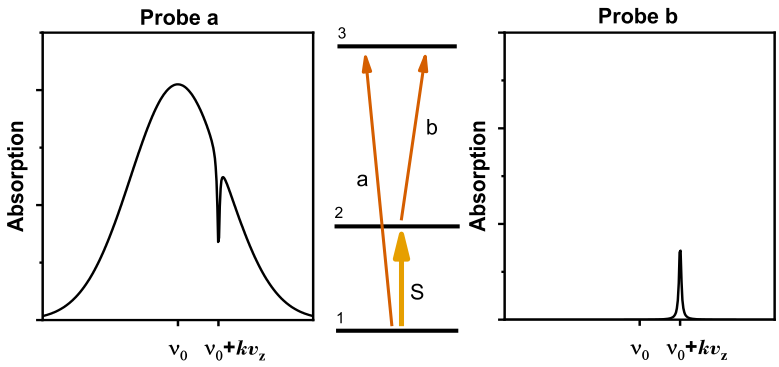

Figure 5.4: Examples of double resonance absorption spectra of the probe beam. The saturating beam (S) is tuned to the side of the transition between states 1 and 2. Probe 'a' measures a V-type transition between the lower state 1 and a third state 3. The absorption spectrum shows a Doppler broadened transition, with a Bennett hole. Probe 'b' measures a ladder-type transition starting from from the higher energy state 2. Assuming that state 2 has no thermal population, the spectrum shows only a narrow line, which is Doppler shifted from the line center according to the Doppler shift of the saturating beam.

In a more complete view, the double resonance line shape is considered to be a combination of the transition starting from the velocity profile modified by the saturator, and a coherent two-photon transition without an intermediate state [101].

When the saturating wave frequency in the laboratory coordinates (ν_S) is fixed over a Doppler profile of the transition $2 \leftarrow 1$, while the probe wave frequency, in the laboratory coordinates (ν_P), is tuned over the transition $3 \leftarrow 2$, the double resonance shows up at the probe wave frequency:

$$\nu_P = \nu_{12} + \nu_{23} - \nu_S - \frac{1}{2\pi}(k_S + k_P)v_z \tag{5.7}$$

It is important to note that the signs of the wave vectors depend on their relative directions. Equations above assume that the saturating wave and the probe wave are propagating in the same directions. If the probe is propagating to the opposite direction, the sign of k_P in equation 5.7 changes and the prefactor in the velocity term changes to $(k_S - k_P)$.

Even if the wavelength of the saturating beam is fixed, it interacts with a distribution of velocities, the width of which is given by the homogeneous width (equation 5.3). This means that the velocity term in equation 5.7 is distributed accordingly. Since the magnitude of the prefactor before the velocity depends on the relative direction between the saturating wave and the probe wave, so does the width of the distribution of the whole velocity term. Because of this, the linewidth of a double resonance transition depends on whether the saturating and probe wave are co-propagating or counter-propagating [102]. The details of the two-photon line shape depend on measurement conditions and the properties of the transition involved, such as the state

lifetimes. For the transitions studied in this thesis, the probe frequency is larger than that of the saturator and moreover, the state lifetimes are comparable to each other. In this case, the double resonance transitions are close to simple Lorentzian peaks in the probe spectrum [103]. The linewidth of the double resonance peak with a co-propagating saturator and probe is given by [104]:

$$2\Gamma_+ = \gamma_3 + \gamma_2(1+G)^{\frac{1}{2}} + \frac{k_\mathrm{P}}{k_\mathrm{S}}(\gamma_1+\gamma_2)(1+G)^{\frac{1}{2}} \tag{5.8}$$

Here, γ_i gives the decay constant for the state i, according to the energy scheme from figure 5.4. The γ parameter is given in the units of frequency, as it is related to the lifetime of the corresponding state by $\gamma = 1/2\pi\tau$. The linewidth with counter-propagating beams is [104]:

$$2\Gamma_- = \gamma_3 + \gamma_1(1+G)^{\frac{1}{2}} + \left(\frac{k_\mathrm{P}}{k_\mathrm{S}} - 1\right)(\gamma_1+\gamma_2)(1+G)^{\frac{1}{2}} \tag{5.9}$$

For the ladder type double resonance absorption, the sub-Doppler linewidth is narrower with counterpropagating saturator and probe.

5.2.1 Cavity ring-down double resonance spectroscopy of C_2H_2

In article **I**, double resonance is used to measure infrared inactive states of acetylene (C_2H_2). Since the vibrational ground state is symmetric with respect to inversion, transitions to other symmetric vibrational states are absent in typical C_2H_2 infrared spectra (see chapter 2). However, a double resonance transition, with an antisymmetric intermediate state, can be used to access symmetric vibrational states. To observe weak double resonance transitions, CRDS was used for detecting the probe absorption. The intensity of the double resonance transition depends on the strengths of the two transitions involved, and therefore, a strong mid-infrared transition was chosen as the first step.

The measurement setup included two light sources to excite the double resonance: a mid-infrared emitting CW-OPO and an external cavity diode laser (ECDL). The CW-OPO was already described in section 5.1.3. The ECDL is a single mode laser, with the emission wavelength tunable between 1520–1570 nm. The ECDL beam was sent through an AOM, which was acting as the optical switch used to initiate the cavity decays. The CW-OPO idler and ECDL beams were superimposed with a dichroic mirror before they were sent through a high-finesse optical cavity. Only the ECDL beam was resonating inside the cavity, while the CW-OPO idler beam was transmitted by the cavity mirrors. The CRDS cavity was filled with a low pressure sample of pure C_2H_2 gas. Figure 5.5 shows a schematic picture of the measurement setup.

Two symmetric C_2H_2 vibrational states were studied using the CRDS measurement system. An already detected band with the normal mode notation $\nu_1 + 2\nu_3$ was used for test measurements and optimization. Subsequently, double resonance transitions to a previously unobserved symmetric state $\nu_1 + \nu_2 + \nu_3 + \nu_4^1 + \nu_5^{-1}$ were measured with the optimized system. The CW-OPO idler wavelength was tuned to resonance with a strong mid-infrared transition. For the test measurements with $\nu_1 + 2\nu_3$, the fundamental transition of the antisymmetric stretching vibration ν_3 was used. The transition wavelength was about 3 µm. The state has a symmetry Σ_u^+, so both the

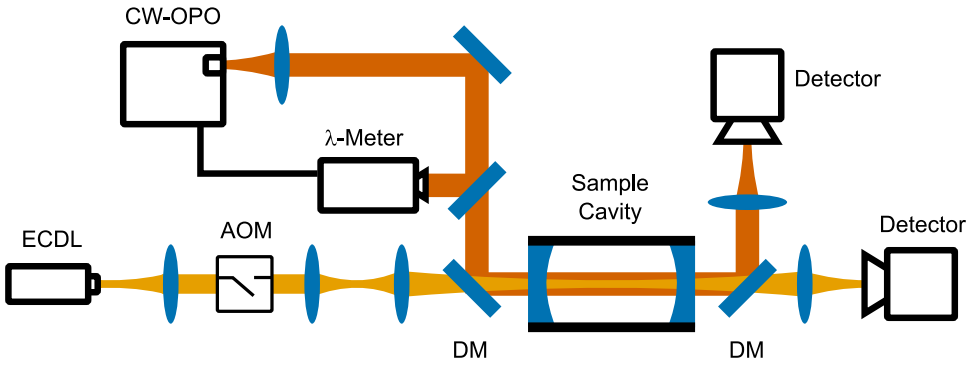

Figure 5.5: Measurement setup from article **I**. A typical CRDS setup with an external cavity diode laser (ECDL) source is modified by adding a mid-infrared CW-OPO. The two beams are superimposed using dichroic mirrors (DM). While the cavity mirrors are highly reflective at the ECDL wavelength, they transmit the mid-infrared beam. The CW-OPO wavelength is monitored with a wavelength meter and controlled to counteract long time scale drifting.

transition $\nu_3 \leftarrow$ GS and $\nu_1 + 2\nu_3 \leftarrow \nu_3$ are allowed by the electric dipole selection rules, which strongly enhances the double resonance transition strength. Additionally, the ν_3 fundamental is one of the strongest vibrational transition of C_2H_2 and the second transition can also be expected to be relatively strong due to the low number of changing vibrational quantum numbers. There is another vibrational state $\nu_2 + \nu_4^1 + \nu_5^{-1}$, with almost equal energy to ν_3. The normal mode notation for the individual states does not represent these resonant states well. Rather, due to a Fermi-type resonance interaction, the observed states are a dyad of mixed states with almost equal contributions from the two states of the normal mode basis set [105]. As a result, even though the transition to the state labeled as $\nu_2 + \nu_4^1 + \nu_5^{-1}$ would be otherwise weak, the resonance with the ν_3 state enhances it to the extent that the transitions $\nu_3 \leftarrow$ GS and $\nu_2 + \nu_4^1 + \nu_5^{-1} \leftarrow$ GS have approximately equal strengths. The latter transition was used as the first step to reach the state $\nu_1 + \nu_2 + \nu_3 + \nu_4^1 + \nu_5^{-1}$.

For the measurements of the state $\nu_1 + 2\nu_3$, the CW-OPO wavelength was tuned to the side of an R-branch line of the ν_3. The CW-OPO wavelength was stabilized with a simple feedback circuit. The wavelength was measured with a wavelength meter, and the CW-OPO pump wavelength was tuned to keep the wavelength meter reading constant. The feedback was effective only against long term drifts, since the wavelength meter updates its reading at a rate of about 1 Hz. Figure 5.6 shows an example of a double resonance absorption spectrum recorded with the measurement setup. The CW-OPO idler wavelength was tuned on the top of the R(15) line of the ν_3 fundamental transition, at the wavenumber of about $3331.206\,\mathrm{cm}^{-1}$. The ECDL wavelength was then scanned over the R(16) line of the transition $\nu_1 + 2\nu_3 \leftarrow \nu_3$. An average of 50 ring-down times was recorded at each wavelength, resulting in the ring-down time spectrum of figure 5.6. The same ring-down spectrum was also recorded without the CW-OPO, resulting in a background spectrum without the sharp double resonance feature. In the context of the double resonance, this background spectrum could be considered as the τ_0 in equation 4.4. The double resonance absorption spectrum

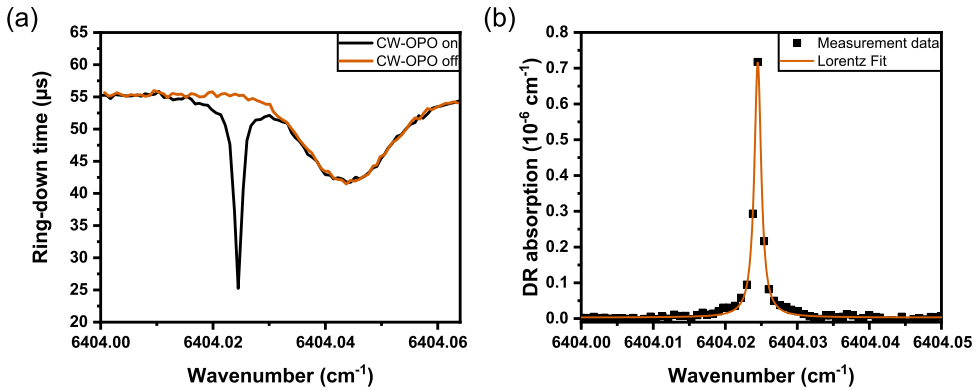

Figure 5.6: Double resonance spectrum. The figure (a) shows the ring-down time as a function of the ECDL wavelength, when it is scanned over the R(16) line of transition $\nu_1 + 2\nu_3 \leftarrow \nu_3$. The black trace shows the spectrum when the CW-OPO is simultaneously exciting the R(15) line of the ν_3 fundamental transition and the yellow line shows the background spectrum when the CW-OPO is off. Figure (b) shows the difference in the absorption between the two traces, together with a Lorentzian line profile fit to the measurement data.

was then calculated as the difference in the attenuation between the two spectra. In this way, the broad linear absorption peak near the double resonance in ring-down spectrum of figure 5.6(a) canceled out in the double resonance absorption spectrum (figure 5.6(b)).

Figure 5.7 shows the double resonance absorption spectrum, when the CW-OPO idler wavelength was slightly off-tuned from the R(15) line center. The ECDL forms a standing wave when it is in resonance with the optical cavity. As a result, it senses the excited velocity distribution, now with nonzero average velocity, with two different orientations of wavevectors, and thus two different Doppler shifts. This results in the appearance of two narrow double resonance peaks in the absorption spectrum, as discussed in the previous section. The two peaks are expected to be asymmetric in their linewidths, as the figure also suggests. However, the asymmetry in the figure is more due to the low resolution of the ECDL wavelength scan and short time scale instabilities in the CW-OPO wavelength, which the slow locking loop cannot correct. For the measurements in article **I**, the line positions were found by tuning the CW-OPO to the center of the $\nu_3 \leftarrow$ GS transition line, and fitting a Lorentzian to the resulting double resonance absorption spectrum. An alternative method would be to purposefully off-tune the CW-OPO idler wavelength from the line center. The two peaks appearing in the ECDL spectrum are symmetrically around the center of the transition line, and calculating the average of their positions gives the line center. However, the former method of finding the line centers was used, because the changes in the CW-OPO wavelength and power between detecting the two off-tuned peaks could degrade the precision of the measurement, and the used locking scheme for the CW-OPO stabilized drifts only on a long time scale.

The optimized setup was used to measure a transition to a previously unobserved

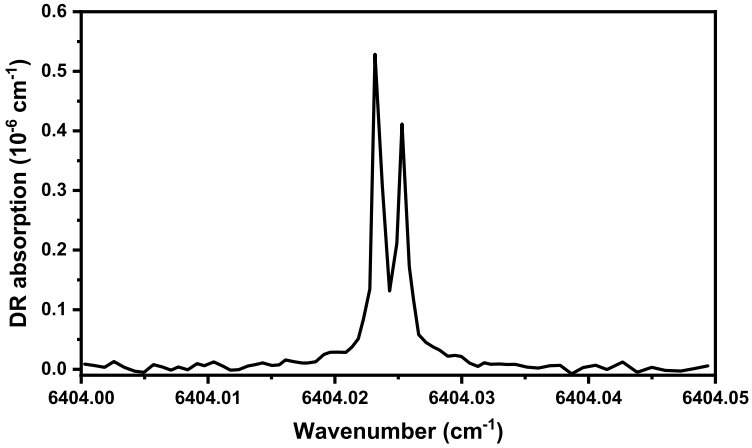

Figure 5.7: Double resonance absorption spectrum showing the two Doppler shifted lines when the CW-OPO idler wavelength is tuned from the center of the R(15) line of the ν_3 fundamental. The off-tuned CW-OPO excites a nonzero velocity component and the counterpropagating waves from the ECDL inside the CRDS cavity sense the molecules with two different wavevectors, resulting in two solutions to the double resonance condition (equation 5.7).

Table 5.1: Rotational parameter fit to the observed energies of the state $\nu_1 + \nu_2 + \nu_3 + \nu_4^1 + \nu_5^{-1}$, with a comparison to a cluster model prediction. The numbers in the parentheses are one-standard errors in the least significant digits.

Rovibrational parameter (cm^{-1})	Fitted parameter	Cluster model [106]
G (cm^{-1})	9775.0018(45)	9774.2
B (cm^{-1})	1.162222(37)	1.162
D ($10^{-6}\,\mathrm{cm}^{-1}$)	3.998(62)	-

vibrational state $\nu_1 + \nu_2 + \nu_3 + \nu_4^1 + \nu_5^{-1}$. The CW-OPO was tuned to a line of the transition $\nu_2 + \nu_4^1 + \nu_5^{-1} \leftarrow GS$. The expected position of the corresponding line of the transition $\nu_1+\nu_2+\nu_3+\nu_4^1+\nu_5^{-1} \leftarrow \nu_2+\nu_4^1+\nu_5^{-1}$ was calculated using the parameters from the cluster model of C_2H_2 [106]. The ECDL wavelength was scanned widely around the calculated position. Ten rovibrational lines of the $\nu_1+\nu_2+\nu_3+\nu_4^1+\nu_5^{-1} \leftarrow \nu_2+\nu_4^1+\nu_5^{-1}$ transition were measured. The lines were approximately equal in intensity to those of the transition $\nu_1 + 2\nu_3 \leftarrow \nu_3$, which was to be expected, since the transition to the intermediate state were of equal strength, and the subsequent transitions shared similar changes in vibrational quanta. The energies of the accessed rotational levels of the newly observed vibrational state were calculated based on the observed transitions, and a linear least squares optimization of the rotational parameters of the state was performed. The fit results are reproduced in table 5.1. They agreed well with those calculated with the cluster model.

5.2.2 Background suppression in double resonance cavity ring-down spectroscopy

With double resonance spectroscopy, subtraction of the linear absorption background is straightforward, since it can be measured by repeating the scan with the probe, after switching the saturating beam off. This is what was done in article **I**. However, the CRDS background level is known to drift slowly over time due to changes in the surrounding conditions. This may lead to problems with the background subtraction if the empty-cavity ring-down time has time to evolve between the scans. In article **IV**, improvements to the background suppression of double resonance CRDS were studied. In the simplest improvement, the probe absorption would be measured alternately with and without the saturator. This would counteract most of the long term drift, leaving only changes on the time scale between the cavity excitation. Since, for example, an AOM can turn off an optical beam in about one microsecond, it is also possible to switch the saturator off during a ring-down decay. Thus, by fitting a modified exponential, where the decay constants changes at the point where the saturator is turned off, it is possible to extract both τ_{RD} and τ_0 from a single cavity decay. This is referred to here as the modulated decay method. It counteracts changes in τ_0 on a shorter time scale as well. However, introducing additional fitting parameters increases the uncertainty of the absorption coefficient calculated from the fitted parameters. This increase was shown in article **IV** to be, theoretically, a factor of about 3.35, relative to the absorption coefficient calculated from the ring-down time of a single exponential fit. However, when compared to the case where the double resonance absorption is calculated as the difference between the decay rates of two separate ring-down decays, the increase is 1.675. This value includes normalization to the measurement time, since measuring two ring-down decays takes twice as long, and an increase in uncertainty, which comes from calculating the difference between two uncorrelated variables.

The modulated decay method was tested experimentally with a measurement setup similar to that shown in figure 5.5. For modulating the CW-OPO power, an additional AOM was introduced after the CW-OPO output. Figure 5.8 shows results from test measurements, where the noise performance of the modulated method was studied. It should be noted that in these tests, there was no sample inside the cavity, and therefore, the results show only the characteristics of the background noise. The results are shown as Allan-Werle deviations, which represents how the standard deviation of the average absorption depends on the averaging time. Figure 5.8(a) compares the noise of the modulated method to that of the absorption calculated from a ring-down time given by a single exponential fit. On a short time scale, the modulated decay led to an increase in noise, as was expected based on the theory. On a long times scale, the ring-down time started to drift, leading to an increase in the noise of the average, but this kind of drift was almost absent in the modulated decay. The increase in uncertainty of the absorption coefficient on a short time scale, relative to a single exponential decay, was found to be a factor of 2, which was slightly less than the theoretical value of 3.35. This would suggest that the noise was not only due to the detector noise, but the ring-down time had some real random variation between the ring-down decays, since this is the effect that the modulated decay method is expected to counteract. This was also demonstrated more rigorously, by inducing excess variation to the ring-down time. The

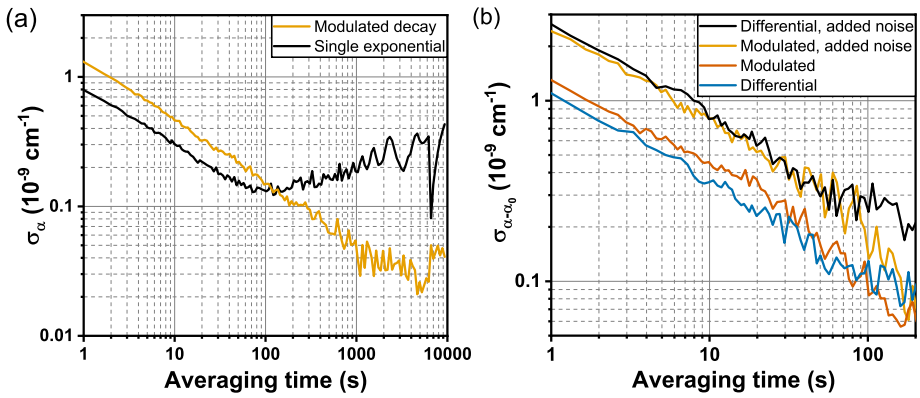

Figure 5.8: Allan-Werle figures for the noise tests of the modulated decay method. In (a), modulated method is compared to a single exponential decay. In (b), the modulated method is compared to calculating the difference between the absorption from two separate single exponential decays. For the 'added noise' traces, extra variation was induced in the ring-down time.

results for this are shown in figure 5.8(b). The modulated decay was compared to the difference between the absorption coefficient from two consecutive single exponential decays. This simulated the case, where one decay was used to extract the signal and the other to obtain the background. Excess noise was added to the ring-down time by modulating the diode laser wavelength with noise and tuning it to a side of an absorption line. This naturally leads to a variation in the ring-down time, because the absorption coefficient changes with the diode laser wavelength. Calculating the absorption coefficient from the modulated decay should suppress most of this noise, because the absorption does not change during the cavity decay, whereas it fully affects the case, where the difference between two ring-down decays are considered. The results show that this was the case. Without the added noise, the modulated decay led to a small increase in the uncertainty as was expected according to the theory. When excess noise was added, the deviation of the modulated decay method fell below the differential method. The added variation in the ring-down time led to an increase in the deviation of the absorption coefficient of about $2.8 \times 10^{-9}\,\mathrm{cm}^{-1}$, over an averaging time of 1 s. This is a large increase in uncertainty, unlikely to appear in typical measurement conditions. However, it should be considered relative to the uncertainty without the added noise. Highly sensitive CRDS setups can have short term noise around $10^{-10}\,\mathrm{cm}^{-1}$. They would be affected by much smaller changes in the ring-down time.

The major advantage of periodic measurement of τ_0 is seen on the long time scale. This was also apparent with the modulated decay method (figure 5.8(a)). After about 100 s, the drift of the ring-down time starts to limit the optimal averaging time, whereas no such time limit was observed with the modulated decay. Unfortunately, this is of limited advantage in the sub-Doppler double resonance measurements performed in this thesis. Technical limitations, such as stability of the light sources and a typical uptime of the locking circuits, tend to limit the useful averaging time below the point

where the modulated decay results in an improvement. The modulated decay could be of use in more specific situations, for example, when measuring broader transitions such as in Doppler broadened stimulated Raman spectroscopy [107].

5.2.3 Frequency comb assisted double resonance spectroscopy of C_2H_2

A major limitation with the measurements in article **I** was the wavelength instability of the light sources. The signal strength of the double resonance transition depends on the offset between the transition frequency and the laser frequency for both of the resonances involved. Thus, any shifts in the wavelengths of either source during the measurement can degrade the line shape and increase the uncertainty of the line center. As a partial remedy to this, the ECDL wavelength in the article **I** was scanned in large steps to keep the measurement time short. The CW-OPO wavelength was also controlled by recording it with a wavelength meter, but the resolution and response time of the meter were limiting the performance of the control loop. In article **III**, a more rigorous locking was established for the CW-OPO wavelength, and the stabilization was also extended to the ECDL wavelength.

Both CW-OPO idler and ECDL wavelengths were referenced against an optical frequency comb. The CW-OPO idler wavelength was stabilized using the mid-infrared DROC as a reference. The locking was implemented in the same way as was described in section 5.1.3. The ECDL wavelength was stabilized against the erbium OFC, which was used to pump the DROC. An auxiliary output of the erbium comb was superimposed with a sampled beam from the ECDL output. Their beat frequency was measured with a fast photodetector. It was sent to a mixer, together with a local oscillator (LO) signal from a signal generator. The mixer outputs the difference frequency between the beat and the LO signals. An integrator controller then tunes the ECDL current, which acts on its wavelength, so that the beat frequency matches the LO signal. The process also locks the phase of the beat signal and therefore, a precise relation between the ECDL and the erbium comb is established. In the article, the linewidth of the beat signal was below 10 Hz.

The stabilized system was used for a high precision measurement of the line R(17) in the transition $\nu_1 + 2\nu_3 \leftarrow \nu_3$. The ECDL wavelength was scanned over the rovibrational transition, while the CW-OPO idler wavelength was stabilized to the side of the Doppler-profile of the line P(18) in the ν_3 fundamental transition. The ECDL wavelength was scanned by tuning the frequency of the LO signal. The phase locked loop varied the ECDL wavelength so that the beat between it and the erbium comb remained locked with the LO. The limitation of this tuning method is that whenever the LO frequency passes over one of the comb lines, or the midpoint between two comb lines, the lock needs to be reestablished. Figure 5.9 shows double resonance absorption spectra of the line R(17) in the transition $\nu_1 + 2\nu_3 \leftarrow \nu_3$. The LO frequency had to be varied in small steps of up to a few hundreds of kHz, for the phase-locked loop to follow it reliably. Therefore, the double resonance spectrum was recorded only near the Doppler shifted peaks, to keep the measurement time reasonable. There were again two peaks, with opposite Doppler shifts, due to the counterpropagating waves that formed the standing wave inside the CRDS cavity. The profiles of the double resonance lines were now resolved and fitted well to Lorentzian functions.

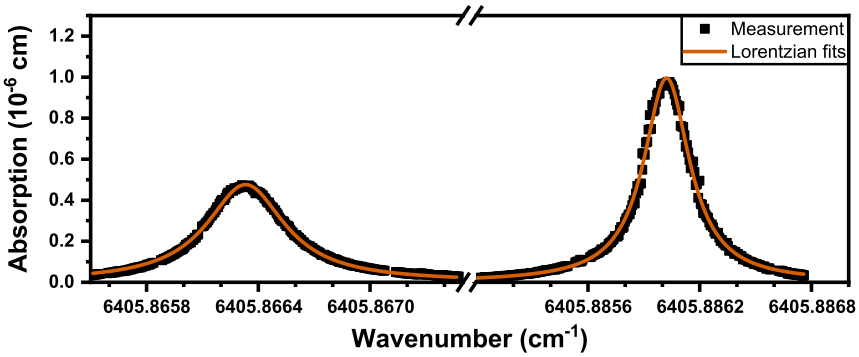

Figure 5.9: Double resonance spectrum measured with frequency stabilized diode laser and CW-OPO.

The difference in the widths of the lines with opposite Doppler shifts is apparent in figure 5.9. The linewidth of the narrower peak was 9.0 MHz and the width of the broader peak was 15.4 MHz at the measurement pressure of 200 mTorr (1 Torr = 133.3 Pa). At this pressure, collisional effects limit the state lifetimes and the homogeneous linewidths of acetylene rovibrational transitions. The decay constants for all acetylene rovibrational states are about $\gamma = 5$ MHz/Torr, nearly independent of the vibrational state [108]. At 200 mTorr, γ is therefore about 1 MHz. Thus, equations 5.9 and 5.8 predict the values 4 and 6 MHz, respectively, for the double resonance linewidths. The CW-OPO linewidth was measured to be about 1.5 MHz, which is comparable to the homogeneous width of the transitions and should be included in the width of the saturated transition. Adding this to the sum $\gamma_1 + \gamma_2$ in equations 5.9 and 5.8 results in linewidths 5.5 and 9 MHz, which are still smaller than the measured values. The saturation parameter was well below unity and would not account for this difference. The measurement was repeated at a pressure of 400 mTorr, which resulted in linewidths of 15.5 and 26.6 MHz. These values are also larger than the predicted values of 9.5 and 15 MHz, when γ is about 2 MHz at 400 mTorr. Many saturation spectroscopy measurements at low pressures have resulted in anomalously large pressure broadening for the width of the Lamb dip [109]. This can be accounted to velocity changing collisions. The pressure broadening linewidth $\gamma = 5$ MHz/Torr is measured from Doppler broadened transition lines at higher pressures. The random velocity changes have little effect on the Doppler broadened line shape [4], except at low pressure, where they can lead to the narrowing of the Doppler linewidth [110]. However, with sub-Doppler measurements, the velocity changing collision can alter the Doppler shift of a molecule and remove it from resonance with the exciting field. This can be considered an effective decrease in the lifetime and should be included in the linewidth γ. Using the model from reference [109], with the value 5 MHz/Torr used for the state lifetimes and other parameters taken from the same reference, the linewidth γ is predicted to be about 2.2 MHz at 200 mTorr and 3.8 MHz at 400 mTorr, when the velocity changing collisions are included. For double resonance peaks, the velocity changing collisions can lead to complicated deviations from the Lorentzian lineshapes [111]. For an approximate description, if the velocity changing collisions

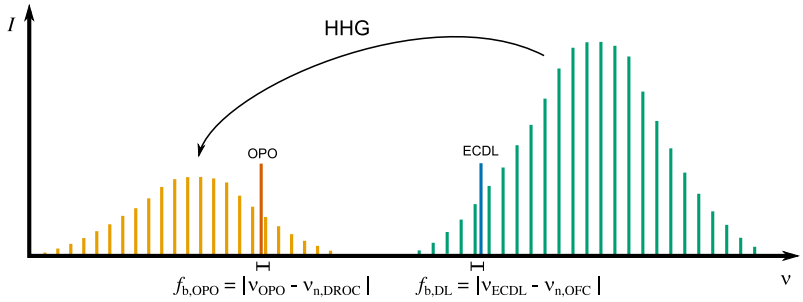

Figure 5.10: Wavelength reference scheme of frequency comb assisted double resonance spectroscopy. The optical frequencies of the CW-OPO and the external cavity diode laser (ECDL) are controlled by measuring their beat frequencies (f_b) against an erbium frequency comb (OFC) and a doubly resonant OPO comb (DROC). Locking loops act on the wavelengths of CW-OPO and diode laser to keep both beat frequencies constant. The DROC is produced by half-harmonic generation from the erbium OFC, resulting in all wavelengths being traceable to the stabilized erbium OFC.

are simply included as additional broadening by using the above values for γ, the predicted linewidths for the double resonance peaks are 9.8 and 15.7 MHz at 200 mTorr, and 16.0 and 25.1 MHz at 400 mTorr, which are close to the measured values.

The wavelength of the ECDL is referenced against a fully stabilized erbium comb. Similarly, the wavelength of the CW-OPO is referenced againts the DROC. The DROC inherits f_{ceo} and f_{rep} from the erbium comb, and is also therefore fully stabilized (see figure 5.10). Thus, both wavelengths are known in reference to the erbium comb f_{ceo} and f_{rep}. These frequency are in turn locked to the SI time standard, which is distributed with GPS. The measurement results can therefore be used to calculate the transition frequencies for both line R(17) of the $\nu_1 + 2\nu_3 \leftarrow \nu_3$ band and line P(18) of the ν_3 fundamental band, against an absolute time standard. The line center of the R(17) line in the $\nu_1 + 2\nu_3 \leftarrow \nu_3$ band is simply at the center point between the two sub-Doppler lines. The separation between the sub-Doppler lines can be used to calculate, which velocity component the CW-OPO is exciting. In this case, since the broader sub-Doppler feature was at lower wavenumber, adding the corresponding Doppler-shift to the recorded CW-OPO idler wavelength gives the line center of the lower transition of the double resonance. The limiting factor in the uncertainty of the results was the stability of the CW-OPO idler wavelength. When the beat note between it and the DROC was recorded with a frequency counter during the measurement, the standard deviation of the beat note was about 90 kHz. This could be considered as the uncertainty of the measured transition frequencies, since the other known sources of uncertainty make only minor contributions. The SNR for the higher of the Doppler-shifted peaks was about 1000, which surpassed the previous measurement setups used to detect the same symmetric vibrational state [99, 112].

Chapter 6

Conclusions

During the course of the work done for this thesis, exceptionally sensitive spectroscopic detection systems have been realized. An infrared-infrared double resonance measurement of acetylene was performed with high sensitivity by combining strong transitions in the mid-infrared region and sensitive detection by near-infrared cavity ring-down spectroscopy. The new detection scheme allowed for an access to a vibrational state of C_2H_2, which had not been previously detected. The generation of novel spectroscopic data can be of use in the development and testing of theoretical models of acetylene. For example, the cluster model of acetylene is based on fitting spectroscopic parameters to experimental data [113]. Ab initio models can often be improved based on experimental results [114]. Furthermore, the double resonance measurement system developed is expected to be readily applicable to other molecules as well. Double resonance allows, for example, a more selective excitation of only a single transition, which can be useful when working with molecules, which possess a crowded infrared spectrum or closely packed fine structures [115]. Double resonance spectroscopy can also be applied to investigate relaxation processes of excited rovibrational states [116]. One major limitation of the double resonance setup was the instabilities of the light sources. This limitation was surpassed by locking the wavelengths using optical frequency combs. With the stabilized sources, sensitivity exceeding the previous setups used to measure similar states was achieved.

This thesis work produced the most sensitive broadband photoacoustic measurement up to date. This was achieved by combining a high-power mid-infrared frequency comb and CEPAS detector. The results demonstrate that the high-power SROC couples well with the broadband CEPAS detection, since it can directly take advantage of the high power spectral density of the SROC. The setup is suitable for the detection of samples with limited availability due to the high sensitivity and small sample volume. The technique was used to measure the first reported infrared spectrum of $^{14}CH_4$. The results have an exciting potential to lead to the development of direct optical detectors for radiocarbon containing methane. The existing optical radiocarbon detectors are limited to $^{14}CO_2$. In principle, such detectors can be used to measure $^{14}CH_4$ concentrations as well, if the sample is first burned to produce CO_2. However, the direct detection of $^{14}CH_4$ would provide specificity to the source of ^{14}C, and in addition, it would require no sample pretreatment. This would be of interest in the

development of compact, field operative detectors. While the frequency comb allows sensitive broadband measurements, the lowest detection limits are reached in line by line measurements using single mode lasers. The next step in development of optical $^{14}CH_4$ detectors would involve a single mode laser or CW-OPO for more sensitive and selective measurements of the $^{14}CH_4$ transition lines to improve the accuracy of the line list. The results of article **IV** will be of assistance in choosing the optimal wavelength range for the CW light source. Increasing the sensitivity of the measurement would also allow resolving many of the lines that were not yet assigned. While the broadband measurements showed promising candidate lines for development of optical $^{14}CH_4$ detectors, it is most likely worthwhile to assign the band more completely in order to find lines with minimal overlap with nearby lines of likely interfering compounds, such as $^{12}CH_4$.

Bibliography

[1] I. Galli, S. Bartalini, R. Ballerini, M. Barucci, P. Cancio, M. De Pas, G. Giusfredi, D. Mazzotti, N. Akikusa, and P. De Natale, "Spectroscopic detection of radiocarbon dioxide at parts-per-quadrillion sensitivity," *Optica* **3**(4), pp. 385–388, 2016.

[2] A. O'Keefe and D. A. G. Deacon, "Cavity ring-down optical spectrometer for absorption measurements using pulsed laser sources," *Review of Scientific Instruments* **59**(12), pp. 2544–2551, 1988.

[3] E. L. Kerr and J. G. Atwood, "The laser illuminated absorptivity spectrophone: A method for measurement of weak absorptivity in gases at laser wavelengths," *Applied Optics* **7**, pp. 915–921, May 1968.

[4] W. Demtroeder, *Laser spectroscopy. Basic concepts and instrumentation*, Springer Series in Chemical Physics, Springer-Verlag Berlin Heidelberg, 1981.

[5] B. A. Paldus and A. A. Kachanov, "An historical overview of cavity-enhanced methods," *Canadian Journal of Physics* **83**(10), pp. 975–999, 2005.

[6] M. D. Levenson and S. S. Kano, *Introduction to Nonlinear Laser Spectroscopy (Second Edition)*, Quantum Electronics–Principles and Applications, Academic Press, 1988.

[7] R. W. Boyd, *Nonlinear Optics*, vol. 3rd, Academic Press, New York, 2008.

[8] M. Vainio and L. Halonen, "Mid-infrared optical parametric oscillators and frequency combs for molecular spectroscopy," *Physical Chemistry Chemical Physics* **18**, pp. 4266–4294, 2016.

[9] Y. Yao, A. J. Hoffman, and C. F. Gmachl, "Mid-infrared quantum cascade lasers," *Nature Photonics* **6**, p. 432, 2012.

[10] I. Vurgaftman, R. Weih, M. Kamp, J. R. Meyer, C. L. Canedy, C. S. Kim, M. Kim, W. W. Bewley, C. D. Merritt, J. Abell, and S. Höfling, "Interband cascade lasers," *Journal of Physics D: Applied Physics* **48**, p. 123001, mar 2015.

[11] S. T. Cundiff and J. Ye, "Colloquium: Femtosecond optical frequency combs," *Reviews of Modern Physics* **75**(1), p. 325, 2003.

[12] A. Foltynowicz, P. Masłowski, T. Ban, F. Adler, K. C. Cossel, T. C. Briles, and J. Ye, "Optical frequency comb spectroscopy," *Faraday Discussions* **150**(0), pp. 23–31, 2011.

[13] R. Holzwarth, A. Nevsky, M. Zimmermann, T. Udem, T. Hänsch, J. von Zanthier, H. Walther, J. Knight, W. Wadsworth, P. Russell, M. Skvortsov, and S. Bagayev, "Absolute frequency measurement of iodine lines with a femtosecond optical synthesizer," *Applied Physics B* **73**, pp. 269–271, Sep 2001.

[14] J. C. J. Koelemeij, B. Roth, A. Wicht, I. Ernsting, and S. Schiller, "Vibrational spectroscopy of HD^+ with 2-ppb accuracy," *Physical Review Letters* **98**, p. 173002, Apr 2007.

[15] B. J. Orr, "Spectroscopy and energetics of the acetylene molecule: dynamical complexity alongside structural simplicity," *International Reviews in Physical Chemistry* **25**(4), pp. 655–718, 2006.

[16] M. Herman, "The acetylene ground state saga," *Molecular Physics* **105**(17-18), pp. 2217–2241, 2007.

[17] K. Leung and R. Lindstedt, "Detailed kinetic modeling of C1 — C3 alkane diffusion flames," *Combustion and Flame* **102**(1), pp. 129–160, 1995.

[18] N. M. Marinov, W. J. Pitz, C. K. Westbrook, A. M. Vincitore, M. J. Castaldi, S. M. Senkan, and C. F. Melius, "Aromatic and polycyclic aromatic hydrocarbon formation in a laminar premixed n-butane flame," *Combustion and Flame* **114**(1), pp. 192–213, 1998.

[19] S. J. Harris and A. M. Weiner, "Determination of the rate constant for soot surface growth," *Combustion Science and Technology* **32**(5-6), pp. 267–275, 1983.

[20] J. Rudolph and D. H. Ehhalt, "Measurements of C2–C5 hydrocarbons over the north atlantic," *Journal of Geophysical Research: Oceans* **86**(C12), pp. 11959–11964, 1981.

[21] K. Didriche and M. Herman, "A four-atom molecule at the forefront of spectroscopy, intramolecular dynamics and astrochemistry: Acetylene," *Chemical Physics Letters* **496**(1), pp. 1–7, 2010.

[22] J. M. C. Rawlings and H. Dhanoa, "Is acetylene essential for carbon dust formation?," *Monthly Notices of the Royal Astronomical Society* **440**, pp. 1786–1793, 03 2014.

[23] S. W. L. Palstra and H. A. J. Meijer, "Biogenic carbon fraction of biogas and natural gas fuel mixtures determined with ^{14}C," *Radiocarbon* **56**(1), p. 7–28, 2014.

[24] J. Mohn, S. Szidat, J. Fellner, H. Rechberger, R. Quartier, B. Buchmann, and L. Emmenegger, "Determination of biogenic and fossil co2 emitted by waste incineration based on 14co2 and mass balances," *Bioresource Technology* **99**(14), pp. 6471–6479, 2008.

[25] K. M. Walter Anthony, P. Anthony, G. Grosse, and J. Chanton, "Geologic methane seeps along boundaries of arctic permafrost thaw and melting glaciers," *Nature Geoscience* **5**, p. 419, 2012.

[26] M.-S. Yim and F. Caron, "Life cycle and management of carbon-14 from nuclear power generation," *Progress in Nuclear Energy* **48**(1), pp. 2–36, 2006.

[27] G. Herzberg, *Infrared and Raman Spectra of Polyatomic Molecules*, Van Nostrand Reinhold, 1945.

[28] L. Rothman, I. Gordon, Y. Babikov, A. Barbe, D. C. Benner, P. Bernath, M. Birk, L. Bizzocchi, V. Boudon, L. Brown, A. Campargue, K. Chance, E. Cohen, L. Coudert, V. Devi, B. Drouin, A. Fayt, J.-M. Flaud, R. Gamache, J. Harrison, J.-M. Hartmann, C. Hill, J. Hodges, D. Jacquemart, A. Jolly, J. Lamouroux, R. L. Roy, G. Li, D. Long, O. Lyulin, C. Mackie, S. Massie, S. Mikhailenko, H. Müller, O. Naumenko, A. Nikitin, J. Orphal, V. Perevalov, A. Perrin, E. Polovtseva, C. Richard, M. Smith, E. Starikova, K. Sung, S. Tashkun, J. Tennyson, G. Toon, V. Tyuterev, and G. Wagner, "The HITRAN2012 molecular spectroscopic database," *Journal of Quantitative Spectroscopy and Radiative Transfer* **130**, pp. 4–50, 2013.

[29] Y. Babikov, I. Gordon, S. Mikhailenko, L. Rothman, and S. Tashkun, "Hitran on the Web." http://hitran.iao.ru/.

[30] K. Shimoda, "Line broadening and narrowing effects," in *High-Resolution Laser Spectroscopy*, K. Shimoda, ed., pp. 11–49, Springer, 1976.

[31] A. E. Siegman, *Lasers*, University Science Books, Sausalito (CA), 1986.

[32] S. E. Harris, "Tunable optical parametric oscillators," *Proceedings of the IEEE* **57**(12), p. 2096, 1969.

[33] L. E. Myers, R. C. Eckardt, M. M. Fejer, R. L. Byer, W. R. Bosenberg, and J. W. Pierce, "Quasi-phase-matched optical parametric oscillators in bulk periodically poled $LiNbO_3$," *Journal of the Optical Society of America B* **12**(11), pp. 2102–2116, 1995.

[34] J. A. Armstrong, N. Bloembergen, J. Ducuing, and P. S. Pershan, "Interactions between light waves in a nonlinear dielectric," *Physical Review* **127**(6), p. 1918, 1962.

[35] R. L. Byer and S. E. Harris, "Power and bandwidth of spontaneous parametric emission," *Physical Review* **168**(3), p. 1064, 1968.

[36] J. Falk, "Instabilities in the doubly resonant parametric oscillator: A theoretical analysis," *IEEE Journal of Quantum Electronics* **7**, pp. 230–235, June 1971.

[37] M. Siltanen, M. Vainio, and L. Halonen, "Pump-tunable continuous-wave singly resonant optical parametric oscillator from 2.5 to 4.4 µm," *Optics Express* **18**, pp. 14087–14092, Jun 2010.

[38] N. Sarukura, Y. Ishida, H. Nakano, and Y. Yamamoto, "cw passive mode locking of a ti:sapphire laser," *Applied Physics Letters* **56**(9), pp. 814–815, 1990.

[39] S. A. Diddams, D. J. Jones, J. Ye, S. T. Cundiff, J. L. Hall, J. K. Ranka, R. S. Windeler, R. Holzwarth, T. Udem, and T. W. Hänsch, "Direct link between microwave and optical frequencies with a 300 THz femtosecond laser comb," *Physical Review Letters* **84**, pp. 5102–5105, May 2000.

[40] E. P. Ippen, H. A. Haus, and L. Y. Liu, "Additive pulse mode locking," *Journal of the Optical Society of America B* **6**, pp. 1736–1745, Sep 1989.

[41] H. A. Haus, E. P. Ippen, and K. Tamura, "Additive-pulse modelocking in fiber lasers," *IEEE Journal of Quantum Electronics* **30**, pp. 200–208, Jan 1994.

[42] R. Roy, P. A. Schulz, and A. Walther, "Acousto-optic modulator as an electronically selectable unidirectional device in a ring laser," *Optics Letters* **12**(9), pp. 672–674, 1987.

[43] C. Spielmann, F. Krausz, T. Brabec, E. Wintner, and A. J. Schmidt, "Femtosecond pulse generation from a synchronously pumped Ti:sapphire laser," *Optics Letters* **16**(15), pp. 1180–1182, 1991.

[44] U. Morgner, F. X. Kärtner, S. H. Cho, Y. Chen, H. A. Haus, J. G. Fujimoto, E. P. Ippen, V. Scheuer, G. Angelow, and T. Tschudi, "Sub-two-cycle pulses from a Kerr-lens mode-locked Ti:sapphire laser," *Optics Letters* **24**, pp. 411–413, Mar 1999.

[45] D. J. Jones, S. A. Diddams, J. K. Ranka, A. Stentz, R. S. Windeler, J. L. Hall, and S. T. Cundiff, "Carrier-envelope phase control of femtosecond mode-locked lasers and direct optical frequency synthesis," *Science* **288**(5466), pp. 635–639, 2000.

[46] R. Holzwarth, T. Udem, T. W. Hänsch, J. C. Knight, W. J. Wadsworth, and P. S. J. Russell, "Optical frequency synthesizer for precision spectroscopy," *Physical Review Letters* **85**, pp. 2264–2267, Sep 2000.

[47] J. K. Ranka, R. S. Windeler, and A. J. Stentz, "Visible continuum generation in air–silica microstructure optical fibers with anomalous dispersion at 800 nm," *Optics Letters* **25**, pp. 25–27, Jan 2000.

[48] F. Tauser, A. Leitenstorfer, and W. Zinth, "Amplified femtosecond pulses from an Er:fiber system: Nonlinear pulse shortening and self-referencing detection of the carrier-envelope phase evolution," *Optics Express* **11**, pp. 594–600, Mar 2003.

[49] L. Xu, C. Spielmann, A. Poppe, T. Brabec, F. Krausz, and T. W. Hänsch, "Route to phase control of ultrashort light pulses," *Optics Letters* **21**, pp. 2008–2010, Dec 1996.

[50] T. R. Schibli, I. Hartl, D. C. Yost, M. J. Martin, A. Marcinkevičius, M. E. Fermann, and J. Ye, "Optical frequency comb with submillihertz linewidth and more than 10 W average power," *Nature Photonics* **2**, p. 355, 2008.

[51] B. R. Washburn, S. A. Diddams, N. R. Newbury, J. W. Nicholson, M. F. Yan, and C. G. Jørgensen, "Phase-locked, erbium-fiber-laser-based frequency comb in the near infrared," *Optics Letters* **29**, pp. 250–252, Feb 2004.

[52] C. R. Phillips, C. Langrock, J. S. Pelc, M. M. Fejer, J. Jiang, M. E. Fermann, and I. Hartl, "Supercontinuum generation in quasi-phase-matched $LiNbO_3$ waveguide pumped by a Tm-doped fiber laser system," *Optics Letters* **36**, pp. 3912–3914, Oct 2011.

[53] A. Hugi, G. Villares, S. Blaser, H. C. Liu, and J. Faist, "Mid-infrared frequency comb based on a quantum cascade laser," *Nature* **492**, p. 229, 2012.

[54] T. J. Kippenberg, R. Holzwarth, and S. A. Diddams, "Microresonator-based optical frequency combs," *Science* **332**(6029), pp. 555–559, 2011.

[55] V. Ulvila, C. R. Phillips, L. Halonen, and M. Vainio, "Frequency comb generation by a continuous-wave-pumped optical parametric oscillator based on cascading quadratic nonlinearities," *Optics Letters* **38**, pp. 4281–4284, Nov 2013.

[56] Y. Kobayashi and K. Torizuka, "Carrier-phase control among subharmonic pulses in a femtosecond optical parametric oscillator," *Optics Letters* **26**, pp. 1295–1297, Aug 2001.

[57] Y. Kobayashi and K. Torizuka, "Measurement of the optical phase relation among subharmonic pulses in a femtosecond optical parametric oscillator," *Optics Letters* **25**, pp. 856–858, Jun 2000.

[58] S. T. Wong, T. Plettner, K. L. Vodopyanov, K. Urbanek, M. Digonnet, and R. L. Byer, "Self-phase-locked degenerate femtosecond optical parametric oscillator," *Optics Letters* **33**, pp. 1896–1898, Aug 2008.

[59] M. Vainio, M. Merimaa, L. Halonen, and K. Vodopyanov, "Degenerate 1 GHz repetition rate femtosecond optical parametric oscillator," *Optics Letters* **37**, pp. 4561–4563, Nov 2012.

[60] N. Leindecker, A. Marandi, R. L. Byer, and K. L. Vodopyanov, "Broadband degenerate OPO for mid-infrared frequency comb generation," *Optics Express* **19**, pp. 6296–6302, Mar 2011.

[61] M. Vainio and L. Halonen, "Stabilization of femtosecond optical parametric oscillators for infrared frequency comb generation," *Optics Letters* **42**, pp. 2722–2725, Jul 2017.

[62] Y. Kobayashi, H. Takada, M. Kakehata, and K. Torizuka, "Optical phase locking among femtosecond subharmonic pulses," *Optics Letters* **28**, pp. 1377–1379, Aug 2003.

[63] D. Butterworth, S. Girard, and D. Hanna, "A simple technique to achieve active cavity-length stabilisation in a synchronously pumped optical parametric oscillator," *Optics Communications* **123**(4), pp. 577–582, 1996.

[64] E. S. Wachman, D. C. Edelstein, and C. L. Tang, "Continuous-wave mode-locked and dispersion-compensated femtosecond optical parametric oscillator," *Optics Letters* **15**, pp. 136–138, Jan 1990.

[65] D. Romanini, A. Kachanov, N. Sadeghi, and F. Stoeckel, "Cw cavity ring down spectroscopy," *Chemical Physics Letters* **264**(3), pp. 316–322, 1997.

[66] J. T. Hodges, J. P. Looney, and R. D. van Zee, "Laser bandwidth effects in quantitative cavity ring-down spectroscopy," *Applied Optics* **35**, pp. 4112–4116, Jul 1996.

[67] J. W. Hahn, Y. S. Yoo, J. Y. Lee, J. W. Kim, and H.-W. Lee, "Cavity ringdown spectroscopy with a continuous-wave laser: calculation of coupling efficiency and a new spectrometer design," *Applied Optics* **38**, pp. 1859–1866, Mar 1999.

[68] Y. He and B. Orr, "Rapid measurement of cavity ringdown absorption spectra with a swept-frequency laser," *Applied Physics B* **79**, pp. 941–945, Dec 2004.

[69] T. Fodes, P. Cermak, J. Rakovsky, M. Macko, J. Kristof, P. Veis, and P. Macko, "Electronic dfb laser switching for continuous wave cavity ring-down spectroscopy," *Electronics Letters* **46**, pp. 523–525, April 2010.

[70] H. Huang and K. K. Lehmann, "Long-term stability in continuous wave cavity ringdown spectroscopy experiments," *Applied Optics* **49**, pp. 1378–1387, Mar 2010.

[71] J. Courtois, K. Bielska, and J. T. Hodges, "Differential cavity ring-down spectroscopy," *Journal of the Optical Society of America B* **30**, pp. 1486–1495, Jun 2013.

[72] S. Kassi and A. Campargue, "Cavity ring down spectroscopy with $5 \times 10^{-13}\,\mathrm{cm}^{-1}$ sensitivity," *The Journal of Chemical Physics* **137**(23), p. 234201, 2012.

[73] G. Giusfredi, S. Bartalini, S. Borri, P. Cancio, I. Galli, D. Mazzotti, and P. De Natale, "Saturated-absorption cavity ring-down spectroscopy," *Physical Review Letters* **104**, p. 110801, Mar 2010.

[74] K. K. Lehmann, "Theoretical detection limit of saturated absorption cavity ring-down spectroscopy (SCAR) and two-photon absorption cavity ring-down spectroscopy," *Applied Physics B* **116**, pp. 147–155, Jul 2014.

[75] L. B. Kreuzer, "Ultralow gas concentration infrared absorption spectroscopy," *Journal of Applied Physics* **42**(7), pp. 2934–2943, 1971.

[76] D. Dumitras, D. Dutu, C. Matei, A. Magureanu, M. Petrus, and C. Popa, "Laser photoacoustic spectroscopy: principles, instrumentation, and characterization," *Journal of Optoelectronics and Advanced Materials* **9**(12), pp. 3655–3701, 2007.

[77] L. B. Kreuzer, *The Physics of Signal Generation and Detection*, pp. 1–25. Academic Press, 1977.

[78] M. Fehér, Y. Jiang, J. P. Maier, and A. Miklós, "Optoacoustic trace-gas monitoring with near-infrared diode lasers," *Applied Optics* **33**, pp. 1655–1658, Mar 1994.

[79] A. A. Kosterev, Y. A. Bakhirkin, R. F. Curl, and F. K. Tittel, "Quartz-enhanced photoacoustic spectroscopy," *Optics Letters* **27**, pp. 1902–1904, Nov 2002.

[80] K. Wilcken and J. Kauppinen, "Optimization of a microphone for photoacoustic spectroscopy," *Applied Spectroscopy* **57**(9), pp. 1087–1092, 2003.

[81] P. Griffiths and J. De Haseth, *Fourier Transform Infrared Spectrometry*, Chemical Analysis: A Series of Monographs on Analytical Chemistry and Its Applications, John Wiley & Sons, 2007.

[82] J. Kauppinen and J. Partanen, *Fourier Transforms in Spectroscopy*, Wiley, 2001.

[83] G. Busse and B. Bullemer, "Use of the opto-acoustic effect for rapid scan Fourier spectroscopy," *Infrared Physics* **18**(5), pp. 631–634, 1978.

[84] C. B. Hirschmann, J. Uotila, S. Ojala, J. Tenhunen, and R. L. Keiski, "Fourier transform infrared photoacoustic multicomponent gas spectroscopy with optical cantilever detection," *Applied Spectroscopy* **64**(3), pp. 293–297, 2010.

[85] T. Mikkonen, C. Amiot, A. Aalto, K. Patokoski, G. Genty, and J. Toivonen, "Broadband cantilever-enhanced photoacoustic spectroscopy in the mid-IR using a supercontinuum," *Optics Letters* **43**, pp. 5094–5097, Oct 2018.

[86] I. Sadiek, T. Mikkonen, M. Vainio, J. Toivonen, and A. Foltynowicz, "Optical frequency comb photoacoustic spectroscopy," *Physical Chemistry Chemical Physics* **20**, pp. 27849–27855, 2018.

[87] W. Yuen and G. Horlick, "Atomic spectrochemical measurements with a Fourier transform spectrometer," *Analytical Chemistry* **49**(9), pp. 1446–1448, 1977.

[88] W. Kutschera, "Applications of accelerator mass spectrometry," *International Journal of Mass Spectrometry* **349-350**, pp. 203–218, 2013.

[89] G. Genoud, M. Vainio, H. Phillips, J. Dean, and M. Merimaa, "Radiocarbon dioxide detection based on cavity ring-down spectroscopy and a quantum cascade laser," *Optics Letters* **40**(7), pp. 1342–1345, 2015.

[90] A. J. Fleisher, D. A. Long, Q. Liu, L. Gameson, and J. T. Hodges, "Optical measurement of radiocarbon below unity fraction modern by linear absorption spectroscopy," *The Journal of Physical Chemistry Letters* **8**(18), pp. 4550–4556, 2017.

[91] A. D. McCartt, T. Ognibene, G. Bench, and K. Turteltaub, "Measurements of carbon-14 with cavity ring-down spectroscopy," *Nuclear Instruments and Methods in Physics Research Section B: Beam Interactions with Materials and Atoms* **361**, pp. 277–280, 2015.

[92] R. S. McDowell, "The ν_3 infrared bands of $C^{12}H_4$ and $C^{13}H_4$," *Journal of Molecular Spectroscopy* **21**(1), pp. 280–290, 1966.

[93] V. Chebotayev and V. Letokhov, "Nonlinear narrow optical resonances induced by laser radiation," *Progress in Quantum Electronics* **4**, pp. 111–206, 1975.

[94] W. R. Bennett, "Hole burning effects in a He-Ne optical maser," *Physical Review* **126**, pp. 580–593, Apr 1962.

[95] W. E. Lamb, "Theory of an optical maser," *Physical Review* **134**, pp. A1429–A1450, Jun 1964.

[96] P. H. Lee and M. L. Skolnick, "Saturated neon absorption inside a 6238 å laser," *Applied Physics Letters* **10**(11), pp. 303–305, 1967.

[97] V. Letokhov, "Saturation spectroscopy," in *High-Resolution Laser Spectroscopy*, K. Shimoda, ed., pp. 95–171, Springer, 1976.

[98] W. K. Bischel, P. J. Kelly, and C. K. Rhodes, "Observation of doppler-free two-photon absorption in the ν_3 bands of CH_3F," *Physical Review Letters* **34**(6), pp. 300–303, 1975.

[99] M. Siltanen, M. Metsälä, M. Vainio, and L. Halonen, "Experimental observation and analysis of the $3\nu_1$ (σ_g) stretching vibrational state of acetylene using continuous-wave infrared stimulated emission," *The Journal of Chemical Physics* **139**(5), p. 054201, 2013.

[100] J. E. Bjorkholm and P. F. Liao, "Resonant enhancement of two-photon absorption in sodium vapor," *Physical Review Letters* **33**(3), pp. 128–131, 1974.

[101] H. R. Schlossberg and A. Javan, "Saturation behavior of a Doppler-broadened transition involving levels with closely spaced structure," *Physical Review* **150**, pp. 267–284, Oct 1966.

[102] H. K. Holt, "Frequency-correlation effects in cascade transitions involving stimulated emission," *Physical Review Letters* **19**(22), pp. 1275–1277, 1967.

[103] N. Skribanowitz, M. S. Feld, R. E. Francke, M. J. Kelly, and A. Javan, "Possibility of a unidirectional laser amplifier produced by monochromatic optical pumping of a coupled Doppler-broadened transition," *Applied Physics Letters* **19**(5), pp. 161–164, 1971.

[104] V. Chebotayev, "Three-level laser spectroscopy," in *High-resolution Laser Spectroscopy*, K. Shimoda, ed., pp. 201–251, Springer, 1976.

[105] J. Vanderauwera, D. Hurtmans, M. Carleer, and M. Herman, "The ν_3 fundamental in C_2H_2," *Journal of Molecular Spectroscopy* **157**(2), pp. 337–357, 1993.

[106] M. Herman, A. Campargue, M. I. El Idrissi, and J. Vander Auwera, "Vibrational spectroscopic database on acetylene, $\tilde{X}\ ^1\Sigma_g^+$ ($^{12}C_2H_2$, $^{12}C_2D_2$, and $^{13}C_2H_2$)," *Journal of Physical and Chemical Reference Data* **32**(3), pp. 921–1361, 2003.

[107] F. V. Englich, Y. He, and B. J. Orr, "Continuous-wave cavity-ringdown detection of stimulated raman gain spectra," *Applied Physics B* **94**(1), pp. 1–27, 2008.

[108] A. L. Utz, J. D. Tobiason, E. Carrasquillo M., M. D. Fritz, and F. F. Crim, "Energy transfer in highly vibrationally excited acetylene: Relaxation for vibrational energies from 6500 to 13 000 cm^{-1}," *The Journal of Chemical Physics* **97**(1), pp. 389–396, 1992.

[109] S. Twagirayezu, G. E. Hall, and T. J. Sears, "Frequency measurements and self-broadening of sub-doppler transitions in the $\nu_1 + \nu_3$ band of C_2H_2," *The Journal of Chemical Physics* **149**(15), p. 154308, 2018.

[110] R. H. Dicke, "The effect of collisions upon the doppler width of spectral lines," *Physical Review* **89**, pp. 472–473, Jan 1953.

[111] P. R. Berman, "Effects of collisions on linear and non-linear spectroscopic line shapes," *Physics Reports* **43**(3), pp. 101–149, 1978.

[112] M. Metsälä, S. Yang, O. Vaittinen, and L. Halonen, "Laser-induced dispersed vibration–rotation fluorescence of acetylene: Spectra of ortho and para forms and partial trapping of vibrational energy," *The Journal of Chemical Physics* **117**(19), pp. 8686–8693, 2002.

[113] M. I. El Idrissi, J. Liévin, A. Campargue, and M. Herman, "The vibrational energy pattern in acetylene (IV): Updated global vibration constants for $^{12}C_2H_2$," *The Journal of Chemical Physics* **110**(4), pp. 2074–2086, 1999.

[114] K. L. Chubb, A. Yachmenev, J. Tennyson, and S. N. Yurchenko, "Treating linear molecule HCCH in calculations of rotation-vibration spectra," *The Journal of Chemical Physics* **149**(1), p. 014101, 2018.

[115] A. Callegari, H. K. Srivastava, U. Merker, K. K. Lehmann, G. Scoles, and M. J. Davis, "Eigenstate resolved infrared–infrared double-resonance study of intramolecular vibrational relaxation in benzene: First overtone of the ch stretch," *The Journal of Chemical Physics* **106**(1), pp. 432–435, 1997.

[116] B. J. Orr, "Collision-induced rovibrational energy transfer in small polyatomic molecules: the role of intramolecular perturbations," *Molecular Physics* **116**(23-24), pp. 3666–3700, 2018.